

ADA 022840

12
B.S.



ISI/TM-78-11.2

June 1979

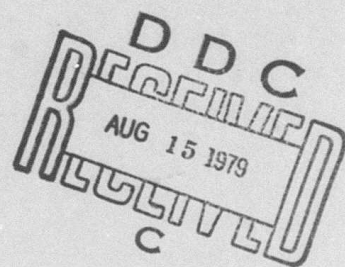
ARPA ORDER NO. 2223

LEVEL ~~VII~~

DARPA NAVY CINCPAC Military Message Experiment

SIGMA Message Service Reference Manual

Version 2.3



Jeff Rothenberg

DDC FILE COPY

This document has been approved
for public release and sale; its
distribution is unlimited.

INFORMATION SCIENCES INSTITUTE

4676 Admiralty Way / Marina del Rey / California 90291
(213) 822-1511

UNIVERSITY OF SOUTHERN CALIFORNIA



79 00 - 123

Security Classification

DOCUMENT CONTROL DATA - R&D

(Security classification of title, body of abstract and indexing annotation must be entered when the overall report is classified)

1. ORIGINATING ACTIVITY (Corporate author) International Business Machines Corporation Data Systems Division, East Fishkill Hopewell Junction, N.Y. 12533		2a. REPORT SECURITY CLASSIFICATION Unclassified
		2b. GROUP
3. REPORT TITLE Lifetime Control in Silicon Through Focused Laser Beam Damage.		
4. DESCRIPTIVE NOTE (If report and inclusive dates) Technical May, 1978 to December, 1978		
5. AUTHOR(S) (First name, middle initial, last name) G. H. Schwuttke and K. H. Yang		
6. REPORT DATE 5 February 1979	7a. TOTAL NO. OF PAGES 82	7b. NO. OF REFS 41
8a. CONTRACT OR GRANT NO. Mod. No. P00095 N00173-76-C-0303	9a. ORIGINATOR'S REPORT NUMBER(S) TR-22.22601	
8b. PROJECT, TASK WORK UNIT NOs 15 WARPA Order-3231	9b. OTHER REPORT NO(S) (Any other numbers that may be assigned this report) 12 85p	
c. DOD ELEMENT	10. DISTRIBUTION STATEMENT 9 Technical rept.	
d. DOD SUBELEMENT	11. SUPPLEMENTARY NOTES 1 May - 31 Dec 78	
12. SPONSORING MILITARY ACTIVITY Advanced Research Projects Agency		
13. ABSTRACT This report consists of two chapters. Chapter I discusses minority carrier lifetime degradation in silicon as a result of 200 Kev argon and 80 Kev silicon implantation. The lifetime degradation is studied for the implantation dose range of 10^{11} to 10^{16} ions/cm². The lifetime degradation is different for argon and silicon implantation. For low argon implantation the decrease in lifetime is impurity controlled. At a higher dose the decrease in lifetime is caused by the argon impurity and by the crystal defects generated by the recrystallization of the amorphous damage layer. For silicon implantations the decrease in lifetime is caused by crystal defects only and is minor up to a dose of 10^{14} Si⁺/cm². Chapter II reports results on buried layer gettering through high energy oxygen and argon implantations. High energy argon gettering depends on the implantation dose. Maximum gettering is obtained for high dose implantation. Oxygen gettering shows no implantation dose dependency. Remarkable gettering efficiencies are obtained for an implantation dose of 10^{11} 0⁺/cm².		

IBM-EF-527407

(U) Unclassified

11th floor Security Classification

79 03 01 401 914
79 03 01 008

JW

Security Classification

14. KEY WORDS	LINK A		LINK B		LINK C	
	ROLE	WT	ROLE	WT	ROLE	WT
Silicon						
Minority Carrier Lifetime						
Implantation						

Unclassified

Security Classification

LIST OF INVESTIGATORS

The project is supervised by Dr. G. H. Schwuttke, Principal Investigator. The following people contributed to the work in the report.

Dr. K. H. Yang Investigator
Dr. H. Kappert Investigator
Dr. G. Sixt Investigator

Mr. C. P. Schneider Technical Support
Mr. C. Hoogendorn Technical Support
Ms. S. Focht Technical Support

The work reported in Chapter II was done jointly with NRL.
Major contributions were made by:

Dr. P. Reid
Dr. P. K. Malmberg

NRL
NRL

Accession For	
NTIS G&I	
DDC TAB	
Unannounced	
Justification	
By _____	
Distribution/ _____	
Availability Code A	
Dist.	Avail and/or special
A	

HIGHLIGHTS

Chapter I

Minority carrier lifetime degradation in silicon, as a result of 200 Kev argon and 80 Kev silicon implantation, is measured after a 1h anneal in dry oxygen or a 30 minute anneal in nitrogen.

The lifetime degradation is studied for the implantation range of 10^{11} to 10^{16} ions/cm². For this range, a lifetime decrease spanning 5 orders of magnitude is observed. The decrease in lifetime is minor for a low implantation dose (10^{11} to 10^{12} ions/cm²). It increases sharply with a higher dose. It levels off for the amorphization dose at a lifetime of approximately 10^{-10} seconds.

The lifetime degradation is different for argon and silicon implantations. For low argon implantations the decrease in lifetime is impurity controlled. At a higher dose the decrease in lifetime is caused by the argon impurity and by the crystal defects generated by the recrystallization of the amorphous layer.

For silicon implantations the decrease in lifetime is caused only by crystal defects. Lifetime degradation due to Si⁺ implantation is only minor up to a dose of 10^{14} Si⁺/cm².

After reaching the amorphization dose ($\sim 5 \times 10^{14} \text{ Si}^+/\text{cm}^2$) the lifetime drops rapidly to the 10^{-10} second level. Correspondingly, the number of crystal defects increases in the annealed implanted layer.

Lifetime recovery experiments, using gettering techniques (ISS), are not successful because they do not anneal out the defect state in the crystal caused by the high implantation (amorphization) dose.

Argon implantation of $> 10^{13} \text{ Ar}^+/\text{cm}^2$ leads to the formation of bubbles in the silicon lattice. It is shown that up to 92% of the implanted argon can be trapped in bubbles. Size and number of argon bubbles increases with implantation dose. However, argon bubbles are shown to have only minor influence on lifetime degradation.

Low concentrations of oxygen, introduced through "knock-on" into the substrate, as a result of implantation through an oxide layer, are found to slow down the degradation of lifetime.

Chapter II

High energy argon and oxygen implantations on wafer backsides improve minority carrier lifetimes-measured by the MOS C-t technique-on wafer front sides.

High energy implantations produce buried damage layers under the silicon surface. Such buried damage layers are resistant to annealing cycles as encountered during standard semiconductor processing. Consequently, they provide more efficient gettering action as compared to damage layers produced by low energy implantations.

High energy argon gettering is found to be dependent on the implantation dose. Maximum gettering efficiency is obtained for high dose implantation ($>10^{14} \text{ Ar}^+/\text{cm}^2$) which leads to the formation of sub-surface amorphous layers.

Oxygen gettering shows no clear dose dependency. A remarkable gettering efficiency is already obtained for an implantation dose of $10^{11} \text{ O}^+/\text{cm}^2$.

TABLE OF CONTENTS

LIST OF INVESTIGATORS	iii
HIGHLIGHTS	ii
CHAPTER I	
MINORITY CARRIER LIFETIME DEGRADATION IN ARGON AND SILICON IMPLANTED SILICON	1
INTRODUCTION	1
EXPERIMENTAL	3
1. Sample Preparation	3
2. Electrical Measurements	4
3. Transmission Electron Microscopy	5
RESULTS	5
1. Minority Carrier Lifetime of Ar ⁺ and Si ⁺ Implanted Silicon	5
a. Ar ⁺ Implanted Silicon	8
b. Si ⁺ Implanted Silicon	9
2. Defect Characterization of Ar ⁺ and Si ⁺ Implanted Silicon	10
a. Ar ⁺ Implanted Silicon	10
b. Si ⁺ Implanted Silicon	21
DISCUSSION	29
1. Minority Carrier Lifetime and Defect Characteristics	29
a. Defect Profile	29
b. Bubble Formation	36
c. Defect Characteristics	37
2. Minority Carrier Lifetime After Ion Implantation	42
a. Low Dose Implantation	43
b. High Dose Si ⁺ Implantation	45
c. High Dose Ar ⁺ Implantation	46

SUMMARY	47
REFERENCES	49
CHAPTER II	
BURIED LAYER GETTERING THROUGH HIGH ENERGY (MEV) ARGON AND OXYGEN IMPLANTATION	52
INTRODUCTION	52
EXPERIMENTAL	53
RESULTS	54
1. Minority Carrier Lifetime Measurements	54
2. Damage Characterization	57
a. X-ray Topography	57
b. Transmission Electron Microscopy Investigation	61
c. Preferential Etching	65
DISCUSSION	67
SUMMARY	70
REFERENCES	73

CHAPTER I

**MINORITY CARRIER LIFETIME DEGRADATION IN ARGON
AND SILICON IMPLANTED SILICON**

MINORITY CARRIER LIFETIME DEGRADATION IN
ARGON AND SILICON IMPLANTED ANNEALED SILICON

INTRODUCTION

To control minority carrier lifetime in silicon for device application recombination centers resulting from chemical impurities and/or crystal imperfections are introduced purposely into the silicon lattice. The most effective centers are those whose energy level is near the intrinsic Fermi level.

Gold is known to have an energy level near the middle of the bandgap and is widely used to achieve lifetime reduction¹. The diffusion rate of gold in silicon is very high and it is not possible to limit lifetime reduction to certain areas of the device if the wafer has to go through additional high temperature treatments.

In a previous paper² the use of cesium, which is a slow diffuser in silicon, as a dopant to achieve controlled reduction of minority carrier lifetime was described. In the present investigation minority carrier lifetime in silicon after argon and silicon implantation is studied. Argon is stable in silicon even after annealing at

temperatures of up to 1050°C and has a deep energy level at 0.5 eV^4 . Thus argon seems very attractive as a dopant to obtain low lifetimes in silicon.

The argon is introduced into the silicon lattice by ion implantation. Ion implantation, however, introduces defect centers into the silicon in addition to the impurities. These defect centers act also as recombination centers^{5,7}. Several papers have been published on minority carrier lifetime degradation in silicon after ion implantation^{1,8-10}. It is known that for implantations below the critical amorphization dose annealing at temperatures of up to $900^{\circ}\text{C}^{9-11}$ removes the implantation damage almost completely and lifetime recovers. For implantations exceeding the amorphization dose only few data on lifetime recovery are available. Davies and Roosild⁹ studied the influence of ion damage on lifetime by implantation of Si^+ and C^+ into silicon. Only partial or no recovery of lifetime was observed.

Lifetime reduction in silicon due to argon implantation is due to the argon and also due to the ion damage. In order to separate these two lifetime degrading effects from each other the microscopical nature of the damage centers must be known. For this reason it is of interest to compare lifetime degradation in silicon after argon implantation with the degradation observed after silicon implantation.

Silicon implantation degrades lifetime only through damage centers. Therefore, silicon implantation effects are also discussed in this paper.

EXPERIMENTAL

Sample Preparation

Czochralski grown, p-type silicon wafers of approximately 1 to 2 $\Omega\text{-cm}$ resistivity, (100) orientation, and 2 1/4 inch in diameter are used. After chemical cleaning, three processing steps are applied to the wafers as follows:

1. Ion implantation - thermal oxidation - annealing (I-O-A),
2. Ion implantation - annealing - thermal oxidation (I-A-O),
3. Thermal oxidation - ion implantation - annealing (O-I-A).

Thermal oxidation is carried out in dry oxygen at 1000°C for 60 minutes and annealing is done in nitrogen at 1000°C for 30 minutes. Ion implantation is performed at 200Kev for Ar^+ and 80 Kev for Si^+ implantation. The ion doses used range from 10^{11} to 10^{16} ions/cm².

After removal of the oxide layer on the backside of the wafers, MOS capacitors are formed on the implanted side. Non-implanted wafers are simultaneously processed as control wafers. Aluminum dots of 0.5mm diameter are evaporated on

the front side and aluminum contacts are made to the backside. A final sintering step for good ohmic contact is made in forming gas at 400°C for 30 minutes.

Before any processing step, three wafers out of each group have their backsides treated with Impact-Sound Stressing (ISS)⁷. This is done in order to see if ISS gettering has any significant effect on lifetime improvement of the implanted wafers.

Electrical Measurements

The minority carrier lifetime in the silicon is determined from the transient response of the MOS capacitors¹². To avoid surface-state charging effects, the MOS capacitors are initially biased into heavy inversion. Subsequently, a depleting negative voltage step is applied to the MOS capacitors. The relaxation of the MOS capacitance with time is monitored. For transient response times of 1 msec to 1 sec an oscilloscope is used, while for times longer than 1 sec the capacitance versus time C(t) curve is plotted on a X-t recorder. The measurement setup used and the computer program for lifetime data as obtained from the C(t) curves are described in Reference 12.

High frequency capacitance-voltage curves are measured at 1 Mhz. From these curves flatband voltages V_{FB} and doping

densities N_D are determined using the computer calculations of Goetzberger .

Transmission Electron Microscopy Investigation

For transmission electron microscopy (TEM) investigations, specimens of 3mm diameter are cut ultrasonically from the implanted wafers. Aluminum dots and oxide layers are removed by etching the wafers in hot H_3PO_4 and HF, respectively. Subsequently, the specimens are thinned by a standard jet-etch technique. The specimens are then investigated either in a JEOL 200A electron microscope operated at 200Kev or in a Philips EM301G electron microscope operated at 100Kev.

RESULTS

1. Minority Carrier Lifetime of Ar^+ and Si^+ Implanted Silicon

The dependence of minority carrier lifetime on implantation dose for Ar^+ and Si^+ implanted silicon is shown in Fig. 1 and 2, respectively. Each data point in these figures represents the mean lifetime averaged from at least three implanted wafers. The mean lifetime of a wafer is obtained from the averaged value of 36 MOS capacitors measured. The mean lifetime for non-implanted control wafers are indicated

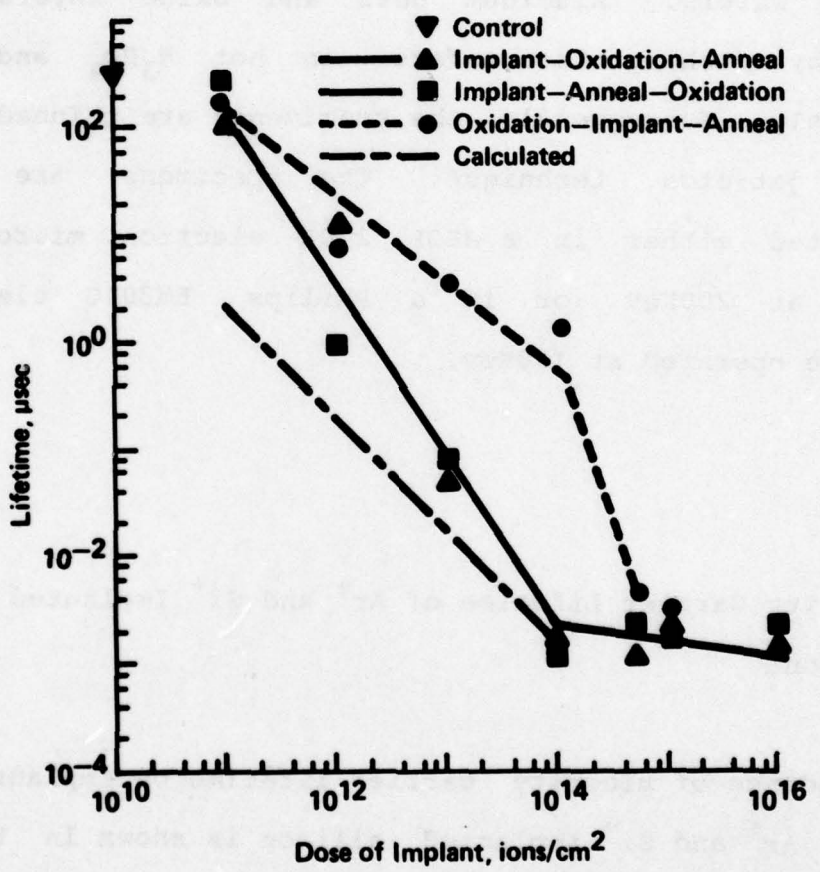


Fig. 1 The dependence of minority carrier lifetime on Ar^+ implantation dose.

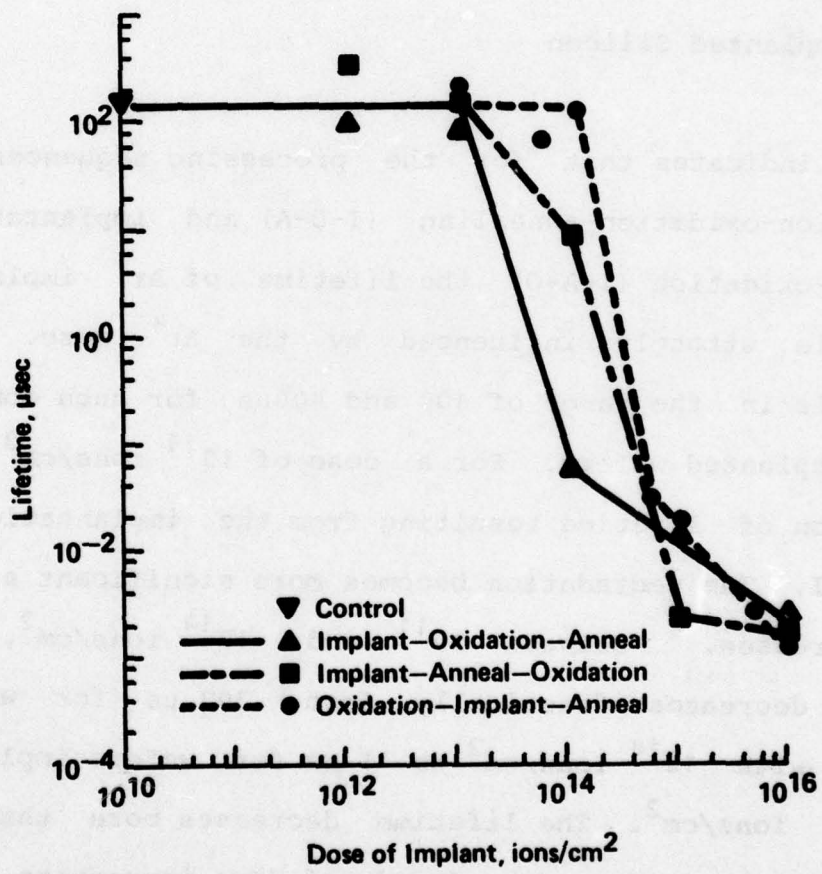


Fig. 2 The dependence of minority carrier lifetime on Si^+ implantation dose.

at the dose of 10^{10} ions/cm². The distribution of the lifetime values in one wafer can spread over 1 to 2 decades for the non-implanted and for the low dose ($<10^{14}$ ions/cm²) implanted samples. The variation of the mean lifetime between the wafers, however, is less than a factor of five. For doses of 10^{14} ions/cm² and higher, the variation decreases to a factor of two.

a. Ar⁺ Implanted Silicon

Figure 1 indicates that for the processing sequences of implantation-oxidation-annealing (I-O-A) and implantation-annealing-oxidation (I-A-O) the lifetime of Ar⁺ implanted silicon is strongly influenced by the Ar⁺ dose. The lifetime is in the range of 100 and 400 μ s for both control and pre-implanted wafers. For a dose of 10^{11} ions/cm², the degradation of lifetime resulting from the implantation is very small. The degradation becomes more significant as the dose increases. Between 10^{11} and 10^{14} ions/cm², the lifetime decreases drastically from 300 μ s for wafers implanted with 10^{14} ions/cm² to 1 ns for wafers implanted with 10^{14} ions/cm². The lifetime decreases more than one order of magnitude for each decade of dose increments. The decrease of lifetime tends to level off for doses higher than 10^{14} ions/cm².

Figure 1 indicates also that pre-annealing before oxidation has no significant effect on the lifetime of Ar^+ implanted silicon.

The use of impact sound-stressing (ISS) gettering has also been investigated. Gettering results only in a small lifetime improvement for wafers implanted with a dose of 10^{11} and 10^{12} ions/cm². At higher doses, the lifetime improvement due to ISS gettering is not significant.

For implantation through oxide with a processing sequence of oxidation-implantation-annealing (O-I-A), Ar^+ implantation causes a smaller degradation of lifetime between 10^{11} and 10^{14} ions/cm². A sharp decrease in lifetime is observed between 10^{14} and 5×10^{14} ions/cm². At higher doses, the lifetime also reaches a value of 1 ns.

b. Si Implanted Silicon

The lifetime data of Si^+ implanted silicon are shown in Fig. 2. The lifetime value is about 100 to 200 μs for both control and pre-implanted wafers. A comparison with Fig. 1 shows different characteristic for the Si^+ versus Ar^+ implanted silicon. Figure 2 indicates that there is no significant degradation in lifetime up to 10^{13} ions/cm² for the I-O-A and the I-A-O cases, and up to 10^{14} ions/cm² for the O-I-A case. A sharp decrease in lifetime occurs between

10^{13} and 10^{14} ions/cm² for the I-O-A and the I-A-O cases, and between 10^{13} and 5×10^{14} ions/cm² for the O-I-A case. The lifetime decreases further with increasing dose and reaches finally a value of 1 ns at 10^{16} ions/cm².

Similar to Ar⁺ implantation, Si⁺ implantation through oxide seems to retard degradation of lifetime. No apparent degradation in lifetime is observed even up to 10^{14} ions/cm². Preannealing before oxidation leads to a pronounced improvement in lifetime at an implantation dose of 10^{14} ions/cm². The lifetime for the I-A-O wafers is about two orders higher than that for the I-O-A wafers.

2. Defect Characterization of Ar⁺ and Si⁺ Implanted Silicon

a. Ar⁺ Implanted Silicon

The characteristics of crystal defects in Ar⁺ and Si⁺ implanted silicon depend strongly on implantation dose, ion species, and on the processing steps. In the as-implanted state, the Ar⁺ implanted layer consists essentially of damage clusters. The size as well as the density of the clusters increase with implantation dose. At and below 10^{12} ions/cm², clusters are not present. At 10^{13} and 10^{14} ions/cm², the size of the clusters is about 50 Å, Fig. 3 (a) and 3(b). Above 10^{14} ions/cm², the clusters start to aggregate and increase in size. At 10^{16} ions/cm²,

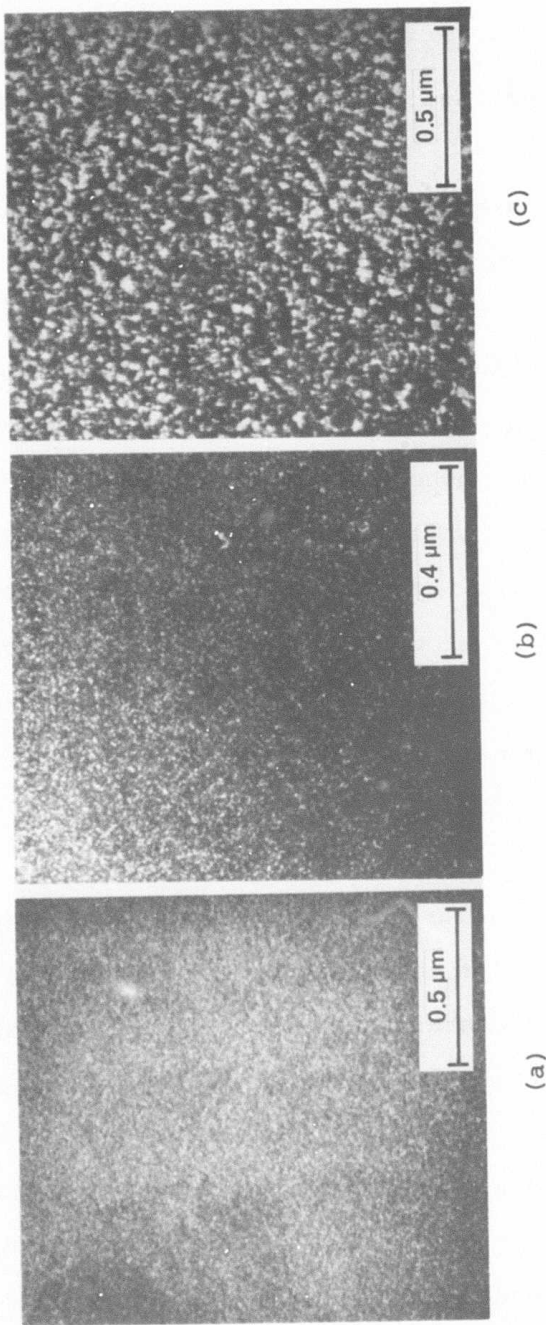


Fig. 3 TEM micrographs showing damage clusters in Ar^+ implanted layer. (a) 10^{13} , (b) 10^{14} and (c) 10^{16} ions/ cm^2 .

the cluster size is about $100 \sim 200\text{\AA}$, Fig. 3 (c). The amorphization dose for Argon implantation is approximately 10^{14} ions/cm² as determined from TEM diffraction patterns.

After oxidation and annealing, the crystal defects undergo a substantial change. This change is also influenced by the implantation dose. This is shown in Figs. 4. At 10^{13} ions/cm², the implanted layer contains mainly spherical argon bubbles $28 \pm 7\text{\AA}$ in size, Fig. 4(a). Damage clusters similar to the argon bubbles are also observed in the as-implanted layer. This indicates that below the amorphization dose, the crystal defects in the implanted layer do not undergo a significant structural change during processing. The stacking fault present in Fig. 4(a) is rarely observed in other areas of the samples and is not representative of the damage.

At the amorphization dose (10^{14} ions/cm²), the implanted layer recrystallizes during oxidation and annealing. The recrystallized layer contains a high density of stacking faults, dislocation half-loops and argon bubbles, Fig. 4(b) and 4(c). As shown in Fig. 4(b), the density of the stacking faults is much higher than that of the loops. The stacking faults lie in {111} planes while the loops are in {110} planes perpendicular to the (001) surface. The nature of the stacking faults can be determined either from the fringe contrast of the faults in contrast or from the

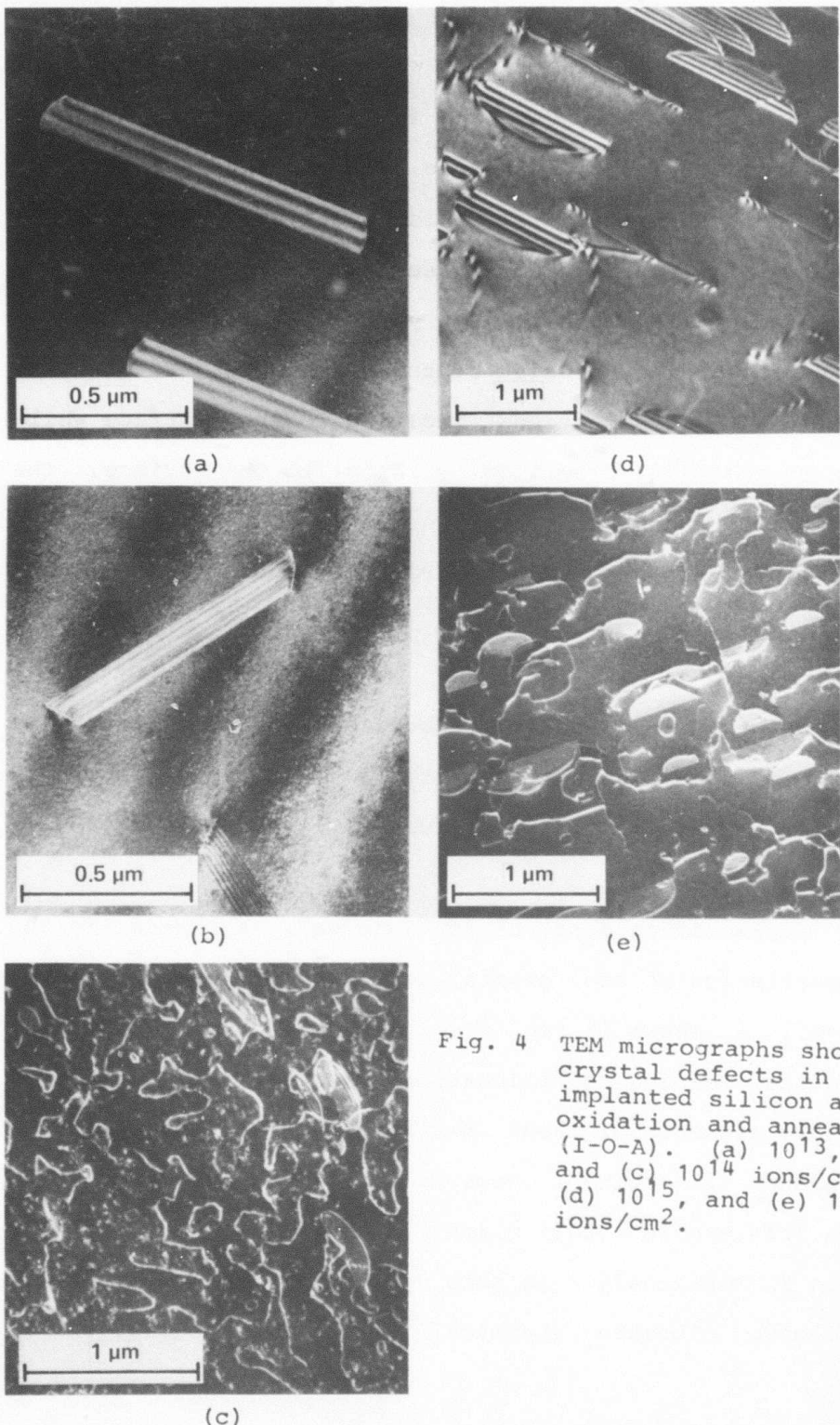


Fig. 4 TEM micrographs showing crystal defects in Ar^+ implanted silicon after oxidation and annealing (I-O-A). (a) 10^{13} , (b) and (c) 10^{14} ions/ cm^2 , (d) 10^{15} , and (e) 10^{16} ions/ cm^2 .

residual contrast of the faults which are out of contrast. Both methods have been used and indicate that the stacking faults are extrinsic in nature. From the analysis of residual contrast, the dislocation loops are determined to be interstitial in nature. These half-loops are unique in so far as they lie in the {110} planes perpendicular to the (001) surface. They consist of three segments, two of which are in the <112> directions inclined to the surface while one is in the <110> direction parallel to the surface. The two inclined segments appear as dot contrast, and the parallel segments show even contrast as shown for the loop, L, in Fig. 4(b).

Argon bubbles can also be recognized. Such defects are resolved by the weak-beam dark-field (WBDF) image shown in Fig. 4(c). The size of these clusters is about $35 \pm 10\text{\AA}$.

At an implantation dose of 10^{15} ions/cm^2 , a change in the characteristics of the crystal defects described so far is observed. As shown in Fig. 4(d), defaulting of some stacking faults leading to dislocations is observed. Glide of the <112> segments of these dislocation half-loop makes the loop plane ill-defined. However, the <110> segment, which has an unfavorable (001) glide plane parallel to the wafer surface is stationary. At this dose ($10^{15}/\text{cm}^2$) the size of the damage clusters (bubbles) increases to $75 \pm 19\text{\AA}$. In

addition to these crystal defects, small dislocation loops, in the range of $0.03 \sim 0.1\mu\text{m}$ in size, are also observed.

At an implantation dose of 10^{16} ions/cm², a further change in the defect characteristics is noticed. As shown in Fig. 4(e), the density of stacking faults is not significantly reduced. The dominant defects are three-dimensional dislocation networks. Examination of stereo-micrographs indicates that the networks are connected by zig-zag dislocation segments and by dislocation segments parallel to the surface. The depth of the parallel segments below the surface is almost equal to the one found for the stacking faults. On the other hand, the zig-zag segments either exit to the surface or stay at an average depth which is equal to the stacking faults depth. In addition to these defects, small dislocation loops and argon bubbles (similar to those observed in the 10^{15} ions/cm² samples) can be seen.

A summary of defect characteristics in Ar⁺ implanted silicon after the processing steps of Ar⁺ implantation-oxidation-N anneal (I-O-A) is given in Table I.

The influence of N₂ pre-annealing on the defect characteristics of Ar⁺ implanted wafers before oxidation is discussed in the following. The defect characteristics for the I-A-O case are shown in Fig. 5. A comparison of Fig. 4 and Fig. 5

TABLE I. Defect Characteristics in Ar⁺ Implanted Silicon Processing
Steps: Ar⁺ Implantation-Oxidation-Anneal (I-O-A)

DOSE Ions/cm ²	ARGON BUBBLES			ST. FAULTS & DISL. HALF-LOOPS		DISL. LOOPS		3-D DISL. NETWORKS	
	Density cm ⁻²	Size Å	Ar in Bubbles %	Density cm ⁻²	Size, μm	Density cm ⁻²	Size, μm	Density cm ⁻²	Size, μm
10 ¹⁴	7x10 ⁹	31±5	1.8	6x10 ⁶	1.2				
5x10 ¹⁴	6x10 ¹⁰	63±13	22.0	4x10 ⁷	0.2~0.6				
10 ¹⁵	2x10 ¹¹	92±30	92.0	8x10 ⁸	0.3~0.5	2x10 ⁸	0.03~0.1		
10 ¹⁶	1x10 ¹¹	100±30		3x10 ⁷	0.3~0.7	3x10 ⁸	0.05~0.1	3x10 ⁸	0.5~1

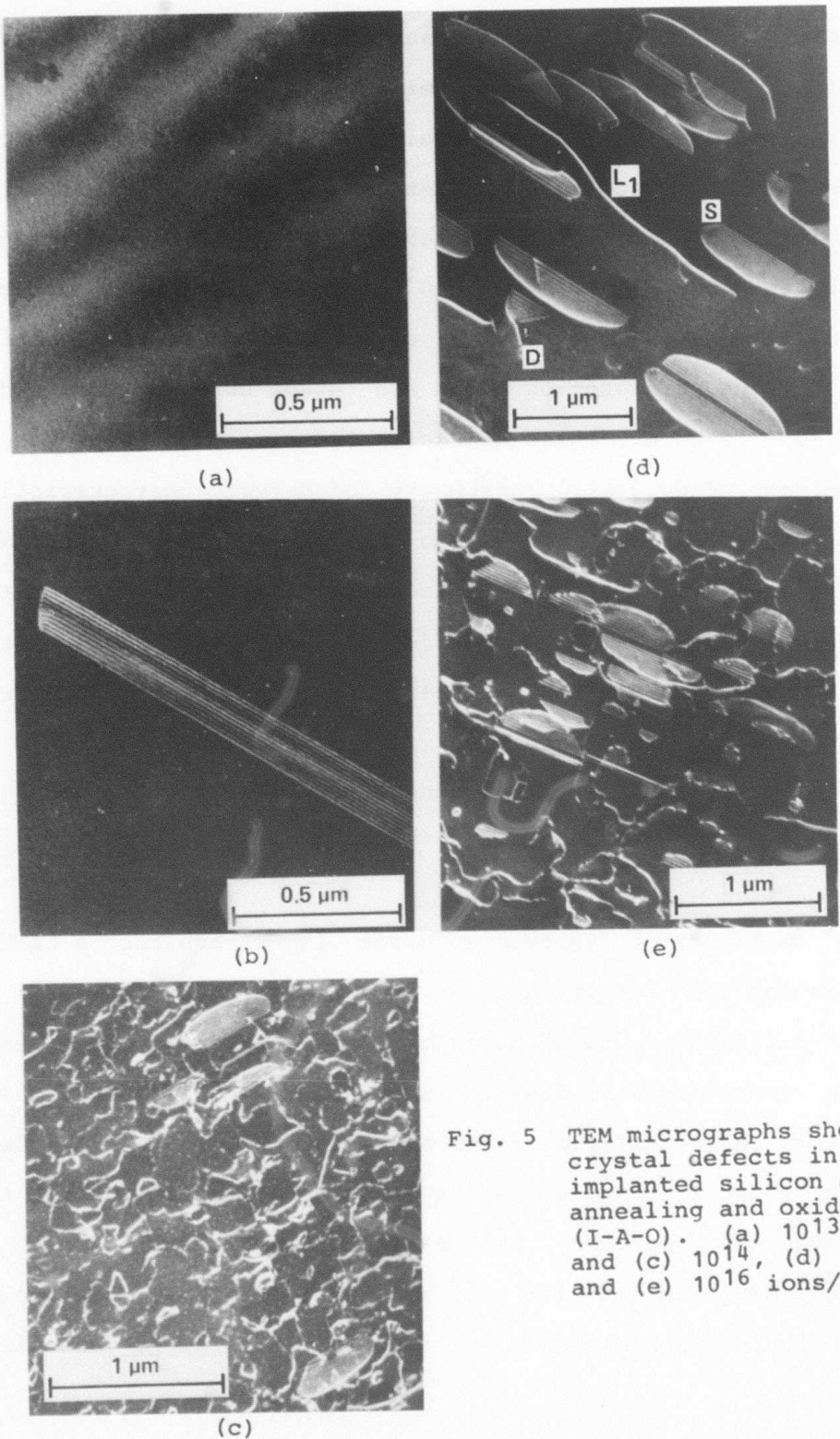


Fig. 5 TEM micrographs showing crystal defects in Ar^+ implanted silicon after annealing and oxidation (I-A-O). (a) 10^{13} , (b) and (c) 10^{14} , (d) 10^{15} , and (e) 10^{16} ions/ cm^2 .

indicates that the N_2 pre-annealing has no significant effect on the defects characteristics. At 10^{13} ions/cm², no damage clusters are resolvable, Fig. 5(a). At the amorphous dose (10^{14} ions/cm²), the major crystal defects are stacking faults, dislocation half-loops, Fig. 5(b), and argon bubbles, Fig. 5(c). At 10^{15} ions/cm², crystal defects consist of a mixture of stacking faults, dislocation half-loops, dislocation loops and argon bubbles, Fig. 5(d). At 10^{16} ions/cm², three-dimensional dislocation loops become dominant, Fig. 5(e). A summary of defect characteristics for the I-A-O case is shown in Table II. A comparison between Table I and II indicates that preannealing of Ar⁺ implanted silicon before oxidation has a negligible effect not only on defect characteristics but also on defect density. The preannealing is also found to have a negligible effect on the generation lifetime as shown in Fig. 1.

Ar⁺ implantation through an oxide layer requires a higher dose for the formation of an amorphous layer. Analysis of TEM diffraction patterns before annealing, indicates that the amorphization dose is about 5×10^{14} ions/cm². The defect characteristics after annealing for the O-I-A wafers are shown in Fig. 6. Below the amorphization dose, the predominant defects are damage clusters as shown in Figs. 6(a) and 6(b) for 10^{13} and 10^{14} ions/cm², respectively. At the amorphization dose (5×10^{14} ions/cm²), annealing

TABLE II. Defect Characteristics in Ar⁺ Implanted Silicon Processing
 Steps: Ar⁺ Implantation-Anneal-Oxidation (I-A-O)

DOSE Ions/cm ²	ARGON BUBBLES		ST. FAULTS & DISL. HALF-LOOPS		DISL. LOOPS		3-D DISL. NETWORKS	
	Density cm ⁻²	Size Å	Density cm ⁻²	Size, μm	Density cm ⁻²	Size, μm	Density cm ⁻²	Size, μm
10 ¹⁴	7x10 ⁸	31±5	6x10 ⁶	1.2				
10 ¹⁵	2x10 ¹¹	92±30	7x10 ⁸	0.2~0.7	2x10 ⁸	0.03~0.1		
10 ¹⁶	2x10 ¹¹	100±30	4x10 ⁷	0.3~0.7	5x10 ⁸	0.05~0.15	5x10 ⁸	0.5~1.0

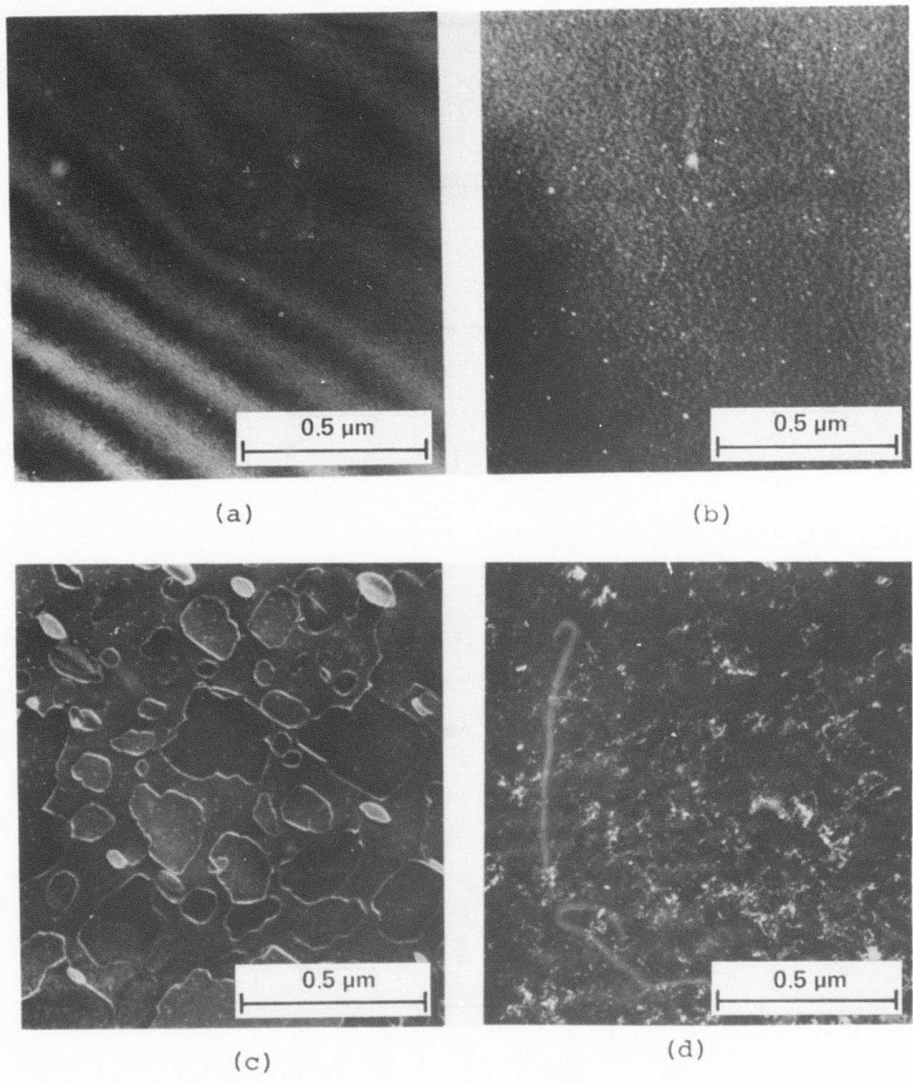


Fig. 6 TEM micrographs showing crystal defects in through oxide Ar^+ implanted silicon (O-I-A). (a) 10^{13} , (b) 10^{14} , (c) 5×10^{14} and (d) 10^{15} ions/ cm^2 .

causes the amorphous layer to recrystallize which generates a high density of stacking faults and dislocation loops, Fig. 6(c). At 10^{15} ions/cm², dislocation loops of two sizes are observed, Fig. 6(d). The defect characteristics for the O-I-A wafers are summarized in Table III.

b. Si⁺ Implanted Silicon

Investigations of as-implanted wafers show that the amorphous rings in the electron diffraction pattern first appear at a dose of 10^{14} ions/cm². The intensity of the amorphous rings in Si⁺ implanted wafers for this dose is much weaker than found in Ar⁺ implanted wafers of the same dose. This indicates that at 10^{14} ions/cm², the degree of amorphousness generated by Si⁺ implantation is much smaller than that generated by Ar⁺ implantation.

For the I-O-A case, no resolvable damage cluster is observed below the amorphization dose. At the amorphization dose (10^{14} ions/cm²), oxidation induces stacking faults. This is shown in Fig. 7(a). The faults are extrinsic in nature. This follows from the fringe contrast of the faults in contrast and also from the residual contrast of the faults which are out of contrast. The size of the faults is quite uniform and is approximately 1.2 μm . The fault density is about 5×10^5 per cm². This is much lower than found for Ar⁺ implantation. At 10^{15} and 10^{16} ions/cm² stacking

TABLE III. Defect Characteristics in Ar⁺ Implanted Silicon Processing
 Steps: Oxidation Ar⁺ Implantation-Anneal (O-I-A)

DOSE Ions/cm ²	ARGON BUBBLES			ST. FAULTS & DISL. HALF-LOOPS		DISL. LOOPS		3-D DISL. NETWORKS	
	Density cm ⁻²	Size Å	Ar in Bubbles %	Density cm ⁻²	Size, μm	Density cm ⁻²	Size, μm	Density cm ⁻²	Size, μm
10 ¹³	1x10 ⁹	17± 6	0.9						
10 ¹⁴	2x10 ¹⁰	37±11	9.8						
5x10 ¹⁴	5x10 ¹⁰	72±17	28.0	5x10 ⁸	0.15	1x10 ⁸	0.1~0.5		
10 ¹⁵	6x10 ¹⁰	72±14	17.6			1x10 ⁹	0.1~0.5	3x10 ⁹	0.05~0.15

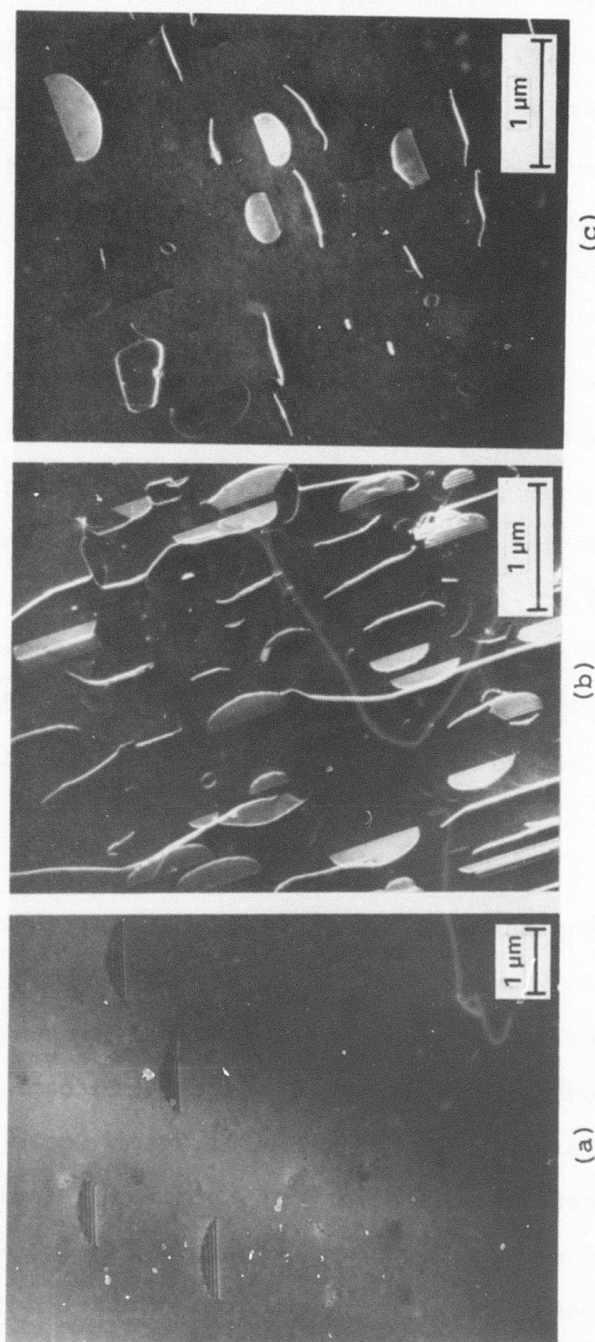


Fig. 7 TEM micrographs showing crystal defects in Si^+ implanted silicon after oxidation and annealing (I-O-A). (a) 10^{14} , (b) 10^{15} and (c) 10^{16} ions/cm².

faults, dislocation half-loops, dislocation loops, and damage clusters are the dominant crystal defects, Fig. 7(b) and 7(c). Surprisingly, the samples implanted with 1×10^{16} ions/cm² have a lower defect density than those implanted with 1×10^{15} ions/cm². The reason for this is presently not understood. The defect characteristics are summarized in Table IV.

Similar to the I-O-A case, no resolvable damage cluster is observed below the amorphization dose for the I-A-O case. At the amorphization dose preannealing causes a reduction in the density of stacking faults, Fig. 8(a). The fault density is estimated to be 5×10^3 per cm². At 10^{15} and 10^{16} ions/cm², preannealing causes most of the stacking faults to default into dislocation half-loops, Fig. 8(b) and 8(c). A summary of the defect characteristics is given in Table V.

As found for Ar⁺ implantation, Si⁺ implantation through oxide also raises the amorphization dose, this time to 5×10^{14} ions/cm². Below the amorphization dose, annealing of the implant-through-oxide wafers does not generate any resolvable crystal defects. At the amorphization dose and higher, annealing causes generation of stacking faults, dislocation loops and damage clusters, as shown in Fig. 9(a) through 9(d). These results indicate that defect characteristics depend on the implantation dose. While

TABLE IV. Defect Characteristics in Si^+ Implanted Silicon Processing
 Steps: Si^+ Implantation-Oxidation-Anneal (I-O-A)

DOSE Ions/ cm^2	ARGON BUBBLES		ST. FAULTS & DISL. HALF-LOOPS		DISL. LOOPS		3-D DISL. NETWORKS	
	Density cm^{-2}	Size μm	Density cm^{-2}	Size, μm	Density cm^{-2}	Size, μm	Density cm^{-2}	Size, μm
10^{14}			5×10^5	1.2				
10^{15}	3×10^{10}	80 ± 30	5×10^8	$0.3 \sim 1.0$	1×10^8	$0.05 \sim 0.1$		
10^{16}	5×10^{10}	100 ± 30	5×10^7	$0.3 \sim 1.0$	3×10^7	$0.05 \sim 0.1$		

TABLE V. Defect Characteristics in Si⁺ Implanted Silicon Processing
 Steps: Si⁺ Implantation-Oxidation-Anneal (I-O-A)

DOSE Ions/cm ²	ARGON BUBBLES		ST. FAULTS & DISL. HALF-LOOPS		DISL. LOOPS		3-D DISL. NETWORKS	
	Density cm ⁻²	Size Å	Density cm ⁻²	Size, μm	Density cm ⁻²	Size, μm	Density cm ⁻²	Size, μm
10 ¹⁴			5x10 ³	1.2				
10 ¹⁵	1x10 ¹⁰	80 ⁺³⁰	5x10 ⁷	0.3~1.0	1x10 ⁷	0.05~0.1		
10 ¹⁶	5x10 ¹⁰	100 ⁺³⁰	5x10 ⁷	0.3~0.8	3x10 ⁷	0.05~0.1		

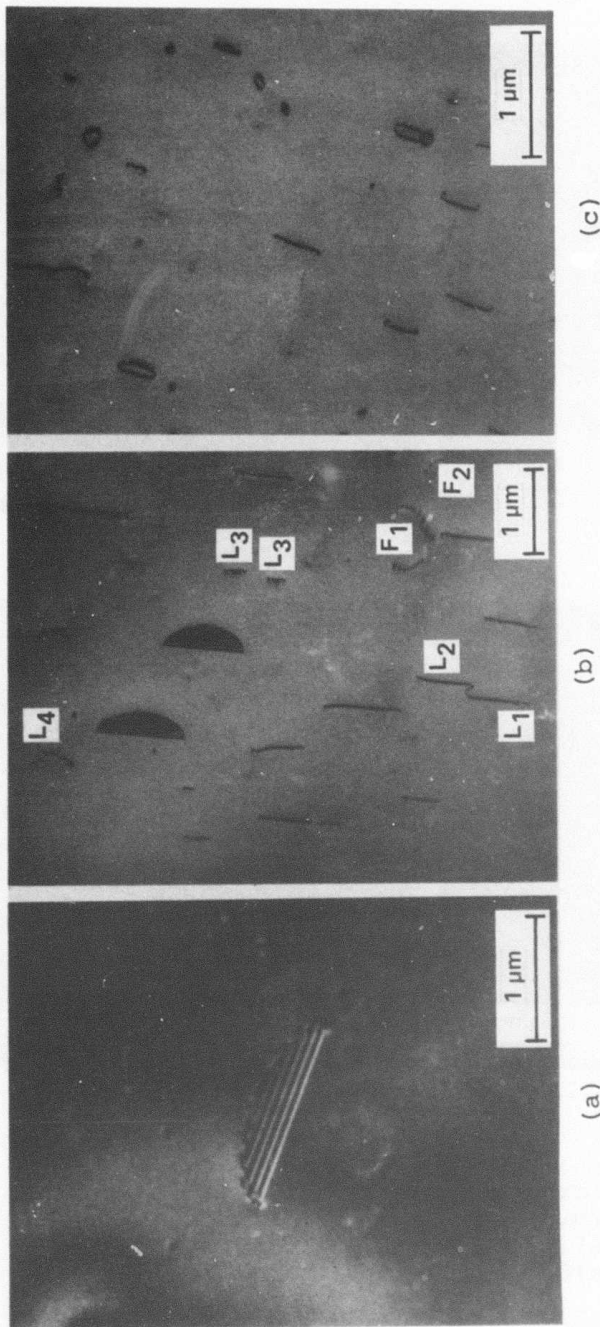


Fig. 8 TEM micrographs showing crystal defects in Si^+ implanted silicon after oxidation and annealing (I-A-O). (a) 10^{14} , (b) 10^{15} and (c) 10^{16} ions/cm².

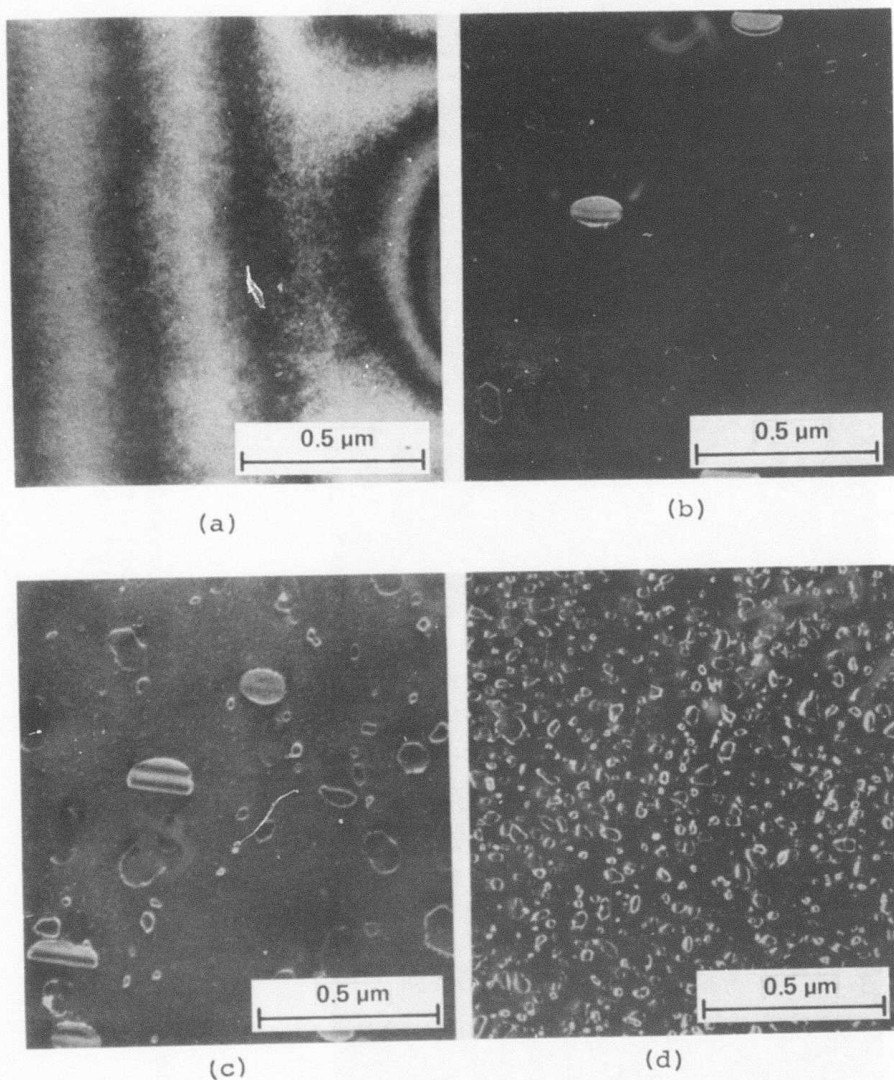


Fig. 9 TEM micrographs showing crystal defects in through oxide Si^+ implanted silicon (O-I-A). (a) 10^{14} , (b) 5×10^{14} , (c) 5×10^{15} and (d) 10^{16} ions/ cm^2 .

stacking faults predominate at 5×10^{14} ions/cm², dislocation loops become the dominant defects at 10^{16} ions/cm². The density of the loops increases, but their size decreases as the implantation dose increases. The defect characteristics for the O-I-A case are summarized in Table VI.

DISCUSSION

1. Minority Carrier Lifetime and Defect Characteristics

a. Defect Profile

The most important event responsible for the nucleation of lifetime degrading defects in the implanted samples is the formation of an amorphous layer during ion bombardment. As the ions penetrate the silicon substrate a damage layer is formed with a maximum defect density at a depth of $R_d = R_p - \sigma_p$, where R_p is the projected range and σ_p the standard deviation.

Once a critical dose is exceeded a continuous amorphous layer is formed at R_p . For both Ar⁺ and Si⁺ irradiation at room temperature the critical amorphization dose is between 1×10^{14} and 5×10^{14} ions/cm². This is verified by TEM diffraction patterns of implanted but unannealed specimens. With increasing ion dose the thickness of the amorphous

TABLE VI. Defect Characteristics in Si⁺ Implanted Silicon Processing
Steps: Oxidation-Si⁺ Implantation-Anneal (O-I-A)

DOSE Ions/cm ²	ARGON BUBBLES		ST. FAULTS & DISL. HALF-LOOPS		DISL. LOOPS		3-D DISL. NETWORKS	
	Density cm ⁻²	Size Å	Density cm ⁻²	Size, μm	Density cm ⁻²	Size, μm	Density cm ⁻²	Size, μm
10 ¹⁴								
5x10 ¹⁴	7x10 ⁹	100	3x10 ⁸	0.15	1x10 ⁸	0.09		
10 ¹⁵	2x10 ⁹	100	4x10 ⁸	0.15	4x10 ⁸	0.09		
5x10 ¹⁵	4x10 ¹⁰	30	5x10 ⁸	0.15	4x10 ⁸	0.1~0.26		
10 ¹⁶	7x10 ¹⁰	30			1x10 ¹⁰	0.01~0.1		

layer increases. The upper crystalline-amorphous interface moves towards the surface and the lower one advances deeper into the silicon crystal.

During a high temperature treatment above 600°C the amorphous layer recrystallizes. The silicon crystal regrowth epitaxially from both amorphous-crystalline interfaces. Residual damage can remain in two regions below the implanted surface. One defect layer remains in the region of the lower crystalline-amorphous interface at a depth of $\sim R_p$ or deeper. The damage nuclei present in this layer grow above 920°C to extrinsic stacking faults and small dislocation loops. Another defect layer is created at the depth of the upper crystalline-amorphous interface¹³. The defect nuclei present in this layer grow above 650°C to larger interstitial dislocation loops and form a sessile dislocation network by dislocation reactions. Whether one or two separate defect layers are finally present depends on the thickness of the amorphous zone before recrystallization.

This behavior explains the depth distribution of the defects found in the samples. The depth distribution as determined from the analysis of TEM stereo micrographs is schematically shown in Fig. 10 for the Ar^+ I-O-A and I-A-O. Figure 11 is for Ar^+ O-I-A while Fig. 12 is for Si^+ O-I-A. The values of R_p and σ_p are obtained from Reference 4.

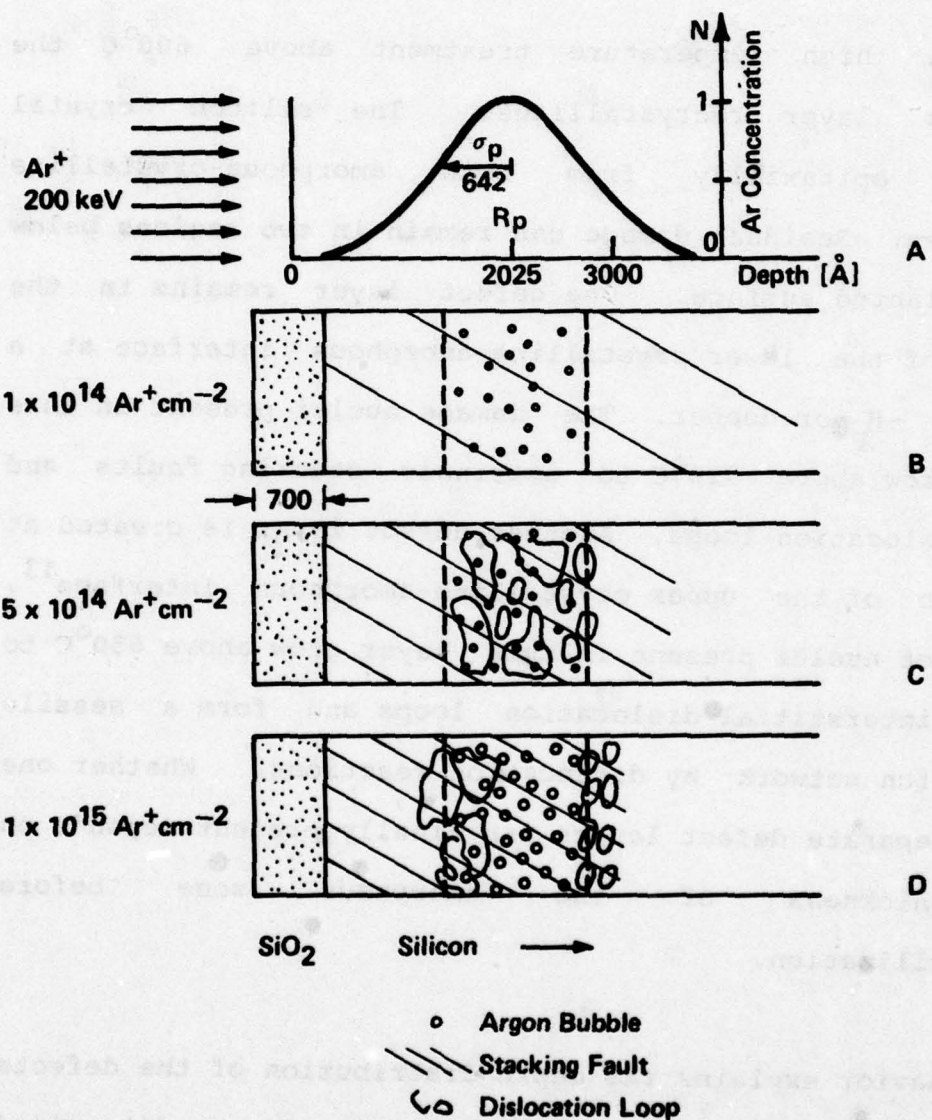


Fig. 10 Schematic drawing of defect profile for Ar^+ I-O-A and I-A-O cases. (a) ion profile (b) 10^{14} , (c) 5×10^{14} and (d) 10^{15} ions/ cm^2 .

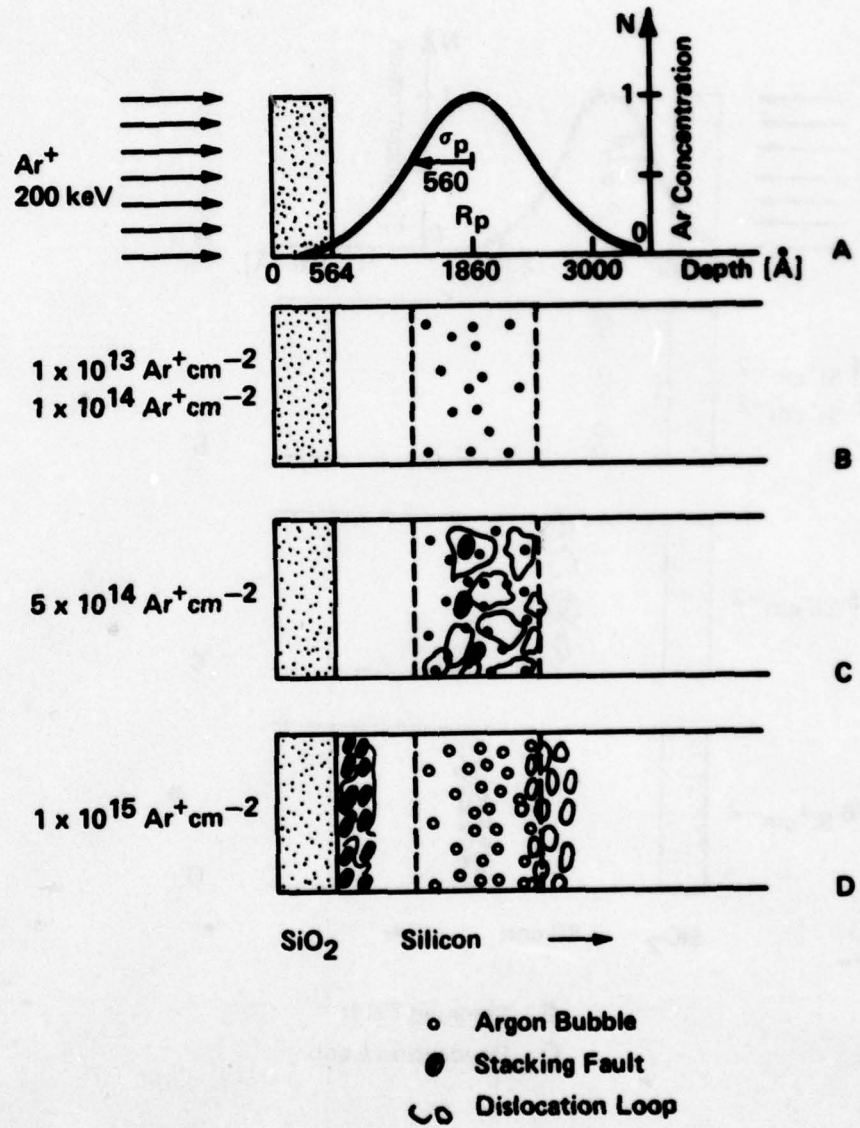


Fig. 11 Schematic drawing of defect profile for through oxide Ar⁺ implantation (0-I-A). (a) ion profile, (b) 10¹³ and 10¹⁴, (c) 5×10¹⁴ and (d) 10¹⁵ ions/cm².

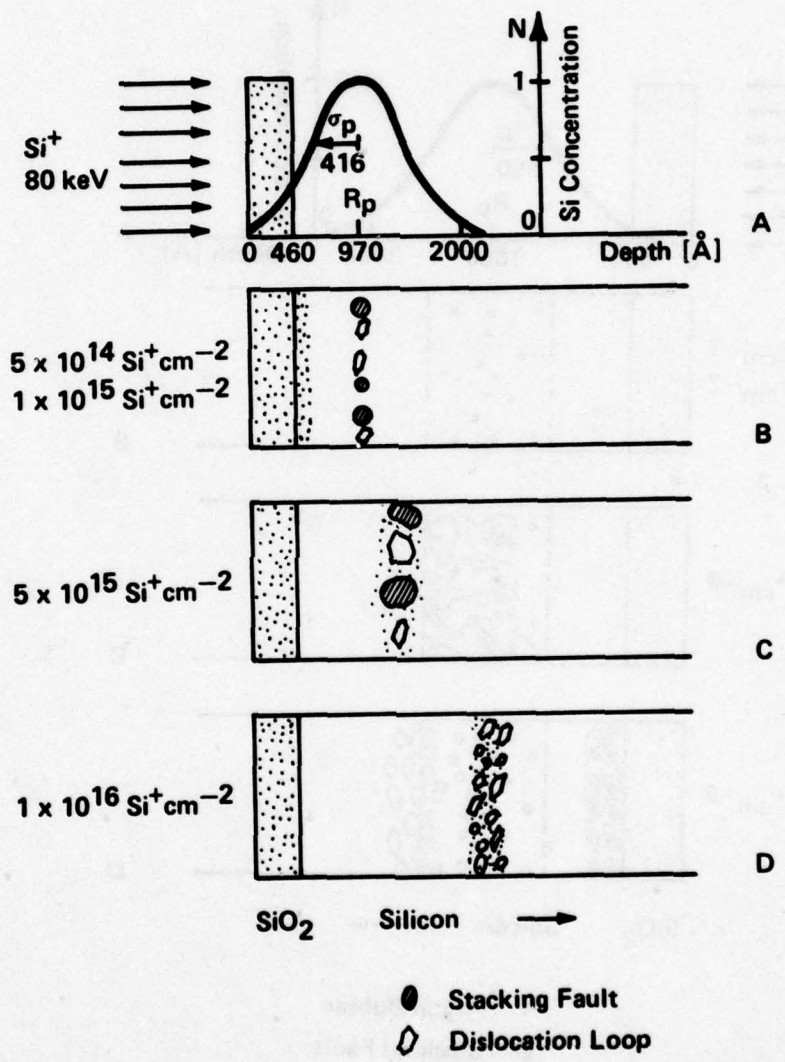


Fig. 12 Schematic drawing of defect profile for through oxide Si^+ implantation (0-I-A), (a) ion profile, (b) 5×10^{14} and 10^{15} , (c) 5×10^{15} and (d) 10^{16} ions/ cm^2 .

After a 30 min. Nitrogen anneal at 1000°C the lower defect layer consists of a high density of dislocation loops of up to $0.2\mu\text{m}$ diameter. The upper defect layer is formed by a dislocation network or larger dislocation loops ($0.2 - 0.5\mu\text{m}$). In the $5 \times 10^{14}\text{ Ar}^+/\text{cm}^2$ implanted samples, Figs. 10(c) and 11(c), both defect layers overlap at a depth equal to R_p below the silicon surface. In the $1 \times 10^{15}\text{ Ar}^+/\text{cm}^2$ implanted samples Figs. 10(d) and 11(d), the two defect layers are separated by about 1000 - 1500Å. In Fig. 11(d), the upper defect layer, consists of small stacking faults of 300 - 600Å diameter, instead of dislocations. This is due to the influence of the SiO_2 -Si interface on fault formation.

In the O-A-I case of Si^+ implanted samples the lower defect layer consists of small stacking faults and dislocation loops. The upper defect layer consists of small damage clusters close to the SiO_2 -Si interface for the 5×10^{14} and $1 \times 10^{16}\text{ Si}^+/\text{cm}^2$ implanted samples. At the higher implantation doses of 5×10^{15} and $1 \times 10^{16}\text{ Si}^+/\text{cm}^2$ the upper crystalline-amorphous interface has reached the surface during the ion bombardment and the epitaxial regrowth starts only from the lower crystalline-amorphous interface. Due to the high implantation dose the depth of this interface is larger than the projected range R_p .

b. Bubble Formation

The argon bubbles observed in the samples of series A and B are found in the most damaged region which extends from $R_p - \sigma_p$ to $R_p + \sigma_p$. Table I, II and III indicate a steady increase of size and density of the argon bubbles with implantation dose. The formation of argon bubbles, however, is related to a critical implantation dose which is approximately 10^{13} to $10^{14} \text{ Ar}^+/\text{cm}^2$. This is somewhat lower than the amorphization dose.

The argon bubbles are formed during the high temperature treatment, when vacancies and argon atoms are mobile. The equilibrium radius r of the spherical bubbles is given by $r = 2\sigma/p$, where σ means the surface energy and p the gas pressure in the bubble. Using a σ -value¹⁵ of 1230 erg/cm^2 , the data measured for the bubble size, the number of argon atoms trapped in a bubble can be calculated by the van der Waals equation of state for non-interacting rigid gas atoms¹⁶. The results are listed in Table I and III. The data indicate that an increasing portion of the implanted argon atoms is trapped in bubbles when the implantation dose is increased. In the I-O-A case at a dose of $10^{15} \text{ ions/cm}^2$, 92% of the implanted argon is trapped within bubbles.

c. Defect Characteristics

The dominant defects in the as-implanted state are damage clusters. Their size and density increase with increasing dose. Below the amorphization dose, the damage clusters are mostly annealed out during high temperature processing. At the amorphization dose, the implanted amorphous layer crystallizes and generates a high density of stacking faults and dislocations. The density of the faults depends on the damage introduced during implantation. The number of faults for Si^+ implantation is lower than that for Ar^+ implantation. For Si^+ implantation, the implantation damage is partially annealed out during pre-annealing. Thus the fault density for the I-A-O case is much lower than for the I-O-A case. For Ar^+ implantation, preannealing has no significant effect on fault density. For low fault densities, the fault size is quite uniform as shown in Fig. 7(a). As the density increases, the variation in fault size becomes significant, Fig. 4(d), 5(d), and 7(b). In addition, interaction between the faults takes place. The interaction results in defaulting leading to dislocation formation. The defaulting mechanisms can be very complicated. Two mechanisms are frequently observed. The first is due to an insufficient supply of silicon interstitials. As the fault density increases, a high concentration of silicon interstitials is required to stabilize the faults. When the supply of interstitials is

insufficient, some faults start to default and transform into prismatic dislocation half-loops. This defaulting mechanism is frequently observed in preannealed samples, Fig. 8(b), and high fault-density samples, Fig. 4(b), 5(b), and 7(b). As can be seen in Fig. 8(b), the half-loops lie in the {110} planes perpendicular to the (001) surface. They consist of two glissile <112> segments inclined to the surface and one sessile <110> segment parallel to the surface. The <112> segments can glide easily in the {111} glide planes. However, the <110> segment has an unfavorable (001) glide plane. When two half-loops are close enough, the interaction of the <112> segments between the two loops can cause the two loops to combine into a larger one. In Fig. 8(b), this interaction is in progress for the two loops, L₁ and L₂. This interaction results into a combination of these two loops into a larger one, such as L₁ in Fig. 5(b). These combined loops can be seen in most of the samples implanted with 10^{15} ions/cm². Perhaps due to both glide and climb, some dislocation half-loops are found to shrink as L₃ in Fig. 8(b).

The second defaulting mechanism is due to the interaction between two intersecting faults. When two faults of opposite inclinations, such as the faults lying in (111) and (11T) planes, (faults F₁ and F₂ in Fig. 8(b)) intersect, defaulting occurs immediately. This results in the

formation of a pair of dislocation half-loops, L_4 and L_5 in Fig. 8(b). When two faults intersect the (001) surface in two perpendicular $\langle 110 \rangle$ directions, such as the (1 $\bar{1}$ 1) and the (111) faults, a Lomer-Cottrell sessile dislocation forms at the intersection, S in Fig. 5(b). When the sessile dislocation reaches the bounding partial dislocation, defaulting takes place and results in a dislocation segment D. This defaulting mechanism has been first reported in one of our previous reports¹⁷. In the work reported in Ref. 17, we intentionally induced a high density of stacking faults by oxidizing ISS damaged wafer surfaces. After a second oxidation, we investigated the interaction between the faults while they grow and intersect. The described defaulting mechanism due to fault intersection was established.

At 10^{15} ions/cm², defaulting becomes more pronounced. As a result, the density of dislocation half-loops increases to a value almost equal to that of stacking faults, Fig. 4(c) and 5(c). Furthermore, interaction between the half-loops progresses relatively easy. This results into lengthening of the half-loops and into the formation of dislocation networks. It can be seen that most of the loops and networks have $\langle 110 \rangle$ edge segments parallel to the (001) surface. Some of them may deviate from this configuration due to a combined motion of glide and climb of the $\langle 110 \rangle$ segments. In addition to these defects, small dislocation

loops (approximately of $0.03\text{--}0.1\mu\text{m}$ in size) can also be seen. These loops are prismatic and lie in $\langle 110 \rangle$ planes. Examination of stereo-micrographs indicates that the loops are positioned at a depth of $0.15\text{--}0.25\mu\text{m}$ below the surface. This depth corresponds to the projected range which is $0.20\mu\text{m}$ for 200 Kev Ar^+ ion implanted into silicon with a standard deviation of $0.05\mu\text{m}$.

For 10^{16} ions/cm^2 , the dominant defects are dislocation networks. As discussed before, the networks are connected by zig-zag dislocation segments and segments parallel to the surface. The depth of the parallel segments below the surface is almost equal to the one found for stacking faults. This suggests that the formation of the networks results from defaulting of stacking faults which leads to dislocations and their interaction. The first stage in the formation of such networks can be seen in Fig. 4(c) and 5(c).

For the O-I-A case, the defect characteristics are somewhat different from those observed for the I-O-A and the I-A-O cases. As shown before, implantation through oxide increases the amorphization dose of silicon to a value of approximately $5 \times 10^{14}\text{ ions/cm}^2$. At 10^{14} ions/cm^2 only damage clusters are observed after annealing. At the amorphization dose, annealing leads to the generation of stacking faults, small, and large dislocation loops,

Fig. 6(b). The size of the stacking faults and of the small loops is about $0.1\mu\text{m}$. The small loops lie in the $\{011\}$ planes inclined to the (001) surface, and are interstitial in nature. The large loops, about $0.5\mu\text{m}$ in size, are mainly connected by $\langle 110 \rangle$ segments parallel to the (001) surface. This gives the over-all impression that the large loops lie in the (001) plane parallel to the surface. We assume that the formation of such loops arises from defaulting of stacking faults which intersect the surface. As discussed before, such defaulting results in the formation of dislocation half-loops. The half-loops consists of two glissile $\langle 112 \rangle$ segments and one sessile $\langle 110 \rangle$ segment. The $\langle 112 \rangle$ segments facilitate interconnection of two neighboring half loops through either lengthening of two parallel half loops or through intersecting two perpendicular half-loops. This leads to the formation of large loops consisting mainly of discrete $\langle 110 \rangle$ sessile segments. The discrete $\langle 110 \rangle$ segments can be seen in Fig. 6(b). They have a length almost equal to that of stacking faults. At 10^{15} ions/cm², three-dimensional dislocation networks similar to that of Fig. 4(e) are formed. We believe that the formation of such dislocation networks arises from the mechanism as discussed above.

2. Minority Carrier Lifetime after Ion Implantation

The minority carrier lifetime t of the MOS capacitors was determined by depleting the surface region and measuring the relaxation of the capacitance. The lifetime is related to the recombination centers of energy E (eV), capture cross section σ (cm^{-2}) and density N_L (cm^{-3}) by equation (1):

$$(1) \quad t = \frac{2\cosh(E_t - E_i)/kT}{V_{th} \sigma N_t}$$

Here V_{th} is the thermal velocity of the carriers and E_i is the intrinsic Fermi level. Within the depletion region of width W the density of recombination centers is given by: $N_t = N_d/W$, where N_d is the defect density per cm^{-2} .

According to the doping densities of 4.6×10^{15} and $1 \times 10^{16} \text{ cm}^{-3}$ the maximum width of the surface depletion layer W_{max} for the p-type samples is calculated to be $0.37 \mu\text{m}$. By comparing this value with the depth profiles presented in Figs. 10, 11 and 12 it is obvious that argon impurities and residual defects are within this region. Therefore both can act as recombination centers and have to be considered as responsible for the reduction of minority carrier lifetime after implantation and high temperature annealing.

As will be shown later, for doses equal or higher than the amorphization dose the decrease in lifetime is mainly related to the residual damage, while for lower doses the impurity effect is dominant. In the following, therefore, the low and high dose implantation are discussed separately.

a. Low-Dose Ar⁺ Implantation

For argon implanted samples with doses smaller than the amorphization dose a steep decrease of generation lifetime t_g of up to 4 orders of magnitude is observed. In these samples the only defects are argon bubbles. The size and density of the bubbles depends on the implantation dose. For the calculation of lifetime degradation both the contribution of the argon dissolved in the silicon lattice as well as the argon bubbles have to be evaluated.

It is reasonable to assume that argon atoms which are trapped in bubbles are not electrically active and that argon bubbles can be treated like voids. In a previous paper the influence of voids on lifetime observed after Cs⁺ implantation was discussed (Ref. 2). In the Cs⁺ study it was found that voids have negligible influence on the generation lifetime.

Similar results are obtained for Ar⁺ implantation. Calculations for argon bubbles indicate that a bubble

density of $1.5 \times 10^{11} \text{ cm}^{-2}$ and a bubble size as large as 92\AA diameter would reduce the generation lifetime only to $1.24\mu\text{sec}$. This leaves the lifetime about three orders of magnitude higher than the measured experimental value of $0.001\mu\text{sec}$.

For the calculation of the minority carrier lifetime dependence on the concentration of dissolved Ar atoms in the silicon lattice an energy level value of $E = 0.5 \text{ eV}^4$ is used in eq. (1). The defect density is given by $N_d = N_I - N_B$, where N_I is the Ar implantation dose and N_B the amount of Ar atoms trapped in bubbles after the heat-treatment as listed in Table I and III. The capture cross-section σ is assumed to be approximately equal to the size of an Ar atom, i.e. $\sigma = 10^{-16} \text{ cm}^2$. The results of these calculations are presented by the dashed line in Fig. 1. The theoretical curve fits the experimental data quite well.

Presently we have no explanation for the shallow step present in the lifetime-vs-dose plot after the through-oxide implantation in Fig. 1 between 10^{12} and $10^{14} \text{ ions/cm}^{-2}$. We speculate that this might be due to the effect of knock-on oxygen atoms which getter deep-level impurities and thus improve the lifetime as observed by other authors¹⁸.

b. High-Dose Si Implantation

Lattice damage without impurity effects is obtained after Si implantation into silicon substrates. Figure 2 shows the lifetime degradation versus implantation dose and Table IV to VI list the defect densities for the Si implanted wafers. A drastic decrease in minority carrier lifetime is observed in samples where defects such as dislocation, loops, and stacking faults are detected.

In order to evaluate the influence of dislocation loops on minority carrier lifetime the dangling bond model is used. According to this model the trap density N_d (last column in Table I - III) can be estimated by $N_d = L_d/b$, where L_d is the total length of the dislocation lines and b is the spacing between dangling bonds at the dislocation. The value of b is assumed to be 3.34\AA for all types of dislocations observed²⁰. The capture cross-section was measured by Glaenzer and Jordan²⁰ and is of the order of $10^{-15} - 10^{-16} \text{ cm}^2$. Energy levels E_t corresponding to 60° and edge dislocations have been investigated experimentally²¹⁻²³ and theoretically²⁴. Various values have been published indicating that the energy levels are located close to the center of the bandgap with $E_t - E_i \leq 0.15 \text{ eV}$.

These data are not accurate enough to make meaningful calculations of t . Consequently, we must be satisfied with an estimate of lifetime dependence on the defect density N_d . For such an estimate, we assume $E_t - E_i = 0$; $v_{th} = 10^7 \text{ cm sec}^{-1}$, and $\sigma = 10^{-15} \text{ cm}^2$. N_d is estimated from Table IV, V and VI. With such data, the estimate results in a reduction of t which is too large by one to two orders of magnitude. However, the estimate does not take into account the Cottrell atmosphere around dislocations which most likely could account for this inaccuracy. The influence of the Cottrell atmosphere on lifetime degradation has been observed by several authors⁶⁻²¹.

c. High-Dose Ar⁺ Implantation

The situation after high-dose Ar⁺ implantation is rather complex. Four different types of recombination centers contribute to the total lifetime degradation: 1) the dangling bonds along the dislocation lines; 2) the Cottrell atmosphere around the dislocations; 3) the dissolved Ar atoms; and 4) the Ar bubbles.

As discussed above, the influence of the Ar bubbles appears small in comparison to the other effects. The influence of the dissolved Ar impurities has been calculated and is plotted in the curves of Fig. 1. It is concluded that the dominant contribution to lifetime degradation is due to the

number of dissolved argon atoms and also due to the number of dislocation.

SUMMARY

Minority carrier lifetime degradation in silicon as a result of 200 KeV argon and 80 KeV silicon implantation is measured after high temperature annealing.

The lifetime degradation is measured for the implantation range of 10^{11} to 10^{16} ions/cm². It is found that the lifetime degradation is ion dose controlled but different for argon and silicon implantations.

For 10^{11} Ar⁺/cm² implantations the decrease is relatively small but increases rapidly with increasing dose and it reaches 5 orders of magnitude for 10^{14} Ar⁺/cm² implantations. The decrease of lifetime levels off for higher doses.

For silicon implantation the effect is similar except that for a silicon dose of up to 10^{14} Si⁺/cm² the degradation is found to be small. For higher implantation the lifetime drops rapidly with implantation dose as found for argon.

The decrease in lifetime due to argon in the dose range of 10^{11} - 10^{14} Ar⁺/cm² is related to the impurity effect of the

implanted argon ions. It is shown that for implantation doses of $10^{13} \text{ Ar}^+/\text{cm}^2$ and higher argon bubbles form in the silicon. The size and density of the argon bubbles increases with the argon implantation dose. Such bubbles can trap up to 92% of the implanted argon. However argon bubbles have only negligible influence on lifetime reduction.

The decrease in generation lifetime caused by argon implanted through an oxide is not as severe as found in samples implanted with argon directly into the silicon substrate.

For silicon implantation doses higher than the amorphization dose ($>10^{14} \text{ Si}^+/\text{cm}^2$) dislocation loops and stacking faults are observed after annealing and the faults are responsible for large lifetime degradations. In such samples the lifetime drops by 5 orders of magnitude as a result of lattice damage. An estimate of the lifetime decrease based on the dangling bonds of dislocations cannot account for such a large decrease. Therefore, it is assumed that the Cottrell atmospheres which form around the dislocations, introduce additional recombination centers which contribute to the lifetime decrease.

In high dose argon implanted samples, i.e. $>1 \times 10^{14} \text{ cm}^2$, lifetime degradation is caused by the argon impurities as well as by the ion damage.

REFERENCES

1. F. N. Schwettmann, J. M. Herman, T. M. Mosman, in "Ion Implantation in Semiconductors", Proceedings of the 4th International Conference 1974, Ed. S. Namba, Plenum Press 1975, p. 697.
2. G. Sixt, H. F. Kappert and G. H. Schwuttke, Phys. Stat. Sol. (a) 43, 119 (1977).
3. T. E. Seidel, R. L. Meek, and A. G. Cullis, J. Appl. Phys. 46, 600 (1975).
4. M. Schulz, App. Phys. 4, 225 (1974); and private communication.
5. A. D. Kurtz, S. A. Kulin, and B. L. Averbach, Phys. Rev. 101, 1285 (1956).
6. H. Lemke, Phys. Stat. Sol. 12, 125 (1965).
7. G. H. Schwuttke, K. F. Yang, and H. F. Kappert, Phys. Stat. Sol. (a) 42, 553 (1977).

8. K. A. Pickar and J. V. Dalton, Rad. Effects 6, 89 (1970).
9. D. E. Davies and S. A. Roosild, Solid St. Electron, 14, 975 (1971).
10. Y. Wada and M. Ashikawa, Jap. J. Appl. Phys. 14, 1405 (1975).
11. K. L. Wang, Appl. Phys. Letters, 29, 700 (1976).
12. W. R. Fahrner and C. P. Schneider, J. Electronics 123, 100 (1976).
13. H. F. Kappert, N. Pfannkuche, K. F. Heidemann, E. te Kaat, to be publ.
14. J. F. Gibbons, W. S. Johnson, and S. W. Mylroie, Projected Range Statistics, 2nd Edition, John Wiley & Sons, Inc. 1975.
15. R. J. Jaccodine, J. Electrochem. Soc. 110, 524 (1963).

16. M. H. Yoo, J. Nucl. Materials 68, 193 (1977).
17. G. H. Schwuttke, "Damage Profiles in Silicon," ARPA Contract No. DAHC15-72-C-0274, Tech. Report No. 7, Part I, Jan., 1976.
18. K. Graff and H. Pieper, J. El. Material 4, 281 (1975).
19. W. Shockley, Phys. Rev. 91, 228 (1953).
20. R. H. Glaenzer and A. G. Jordan Sol. St. Electronics 12, 247 (1969).
21. M. C. Collet, J. Electrochem. Soc. 117, 259 (1970).
22. H. J. Kos and D. Neubert, Phys. Stat. Sol. (a) 44, 259 (1977).
23. W. Mobius and D. Neubert, Verhandl. DPG (VI) 8, 257 (173).
24. W. Schroter and R. Labusch, Phys. Stat. Sol. 36, 539 (1969) R. Labusch and W. Schroter, Inst. Phys. Conf. Ser. No. 23, 56 (1975).

CHAPTER II

BURIED LAYER GETTERING THROUGH HIGH ENERGY (MEV) ARGON AND OXYGEN IMPLANTATION

BURIED LAYER GETTERING THROUGH HIGH ENERGY (Mev)
ARGON AND OXYGEN IMPLANTATION

INTRODUCTION

Argon implantation damage has been used as an effective gettering agent (1-5). The gettering ability arises from the lattice disorder introduced by the implantation (3). For gettering purposes argon implantation is frequently done at 100 Kev. The result is a damage layer approximately 1000\AA thick. Such shallow damage layers recrystallize quickly during high temperature semiconductor processing. For example, a 1 hour oxidation step at 1000°C anneals the damage layer almost completely. Indications are that the gettering action of such thin surface layers ceases after the first oxidation.

Recently, it has been shown that pre-base Ar gettering is less effective than pre-emitter gettering (4). This may relate to the more or less total recrystallization of the damage layer during the base diffusion.

For more effective ion damage gettering subsurface damage layers offer an interesting potential. Such layers, produced through 1 or 2 Mev ions have been shown to recrystallize slowly during high temperature heat treatments

(Ref. 6,7,8). In this study, the potential of buried layer gettering is evaluated.

EXPERIMENTAL

Buried layers are generated by implantation of 1 Mev Ar⁺ and 2 Mev O⁺. These two ions have been shown to be most effective in gettering intentionally copper and gold contaminated silicon devices (3). To implant the ions, a Van der Graaff generator is used. The ions are driven into the Van der Graaff generator with the help of a variable voltage probe. Emerging from the accelerator, the ions drift into a magnetic analysing system. Here the ions are bent 90 degrees into the exit port. The ion beam leaving the analyzer implants a square area on a silicon wafer mounted for backside implantation. The implanted area is 1 1/4" square and located in the middle of a 2 1/4 inch wafer. Thus, implanted versus non-implanted areas can be compared on each single wafer.

The silicon wafers are of (100) surface orientation and are boron-doped to a resistivity of 2 ohm-cm. After ion implantation, MOS capacitors are fabricated on the wafer frontside. The minority carrier lifetime in the silicon is then determined from the transient response of the MOS capacitors (Ref. 15). At least 30 capacitors positioned over the implanted square area and 18 capacitors positioned

over the non-implanted area are measured on the frontside of the wafer. A comparison of the lifetime data obtained from the capacitors positioned over the implanted area and over the non-implanted area allows one to evaluate the efficiency of damage gettering on a single wafer. The implantation dose used ranges from 10^{11} to 10^{16} ions/cm². Two wafers are always implanted with the same dose.

The implantation damage before and after annealing is characterized through x-ray topography and transmission electron microscopy. The x-ray topographs are recorded using Mo Ka radiation. The transmission electron microscopy is performed with a 200 Kev electron microscopy.

RESULTS

Minority Carrier Lifetime Measurements

Figures 1 and 2 show the lifetime values obtained from wafers implanted with 1MeV Ar⁺ and 2MeV O⁺. The lifetime values obtained inside and outside the implanted wafer area are shown for comparison side by side in Figs. 1,2. The values are averaged values obtained from at least 30 MOS capacitors inside and from 18 capacitors outside the implanted area.

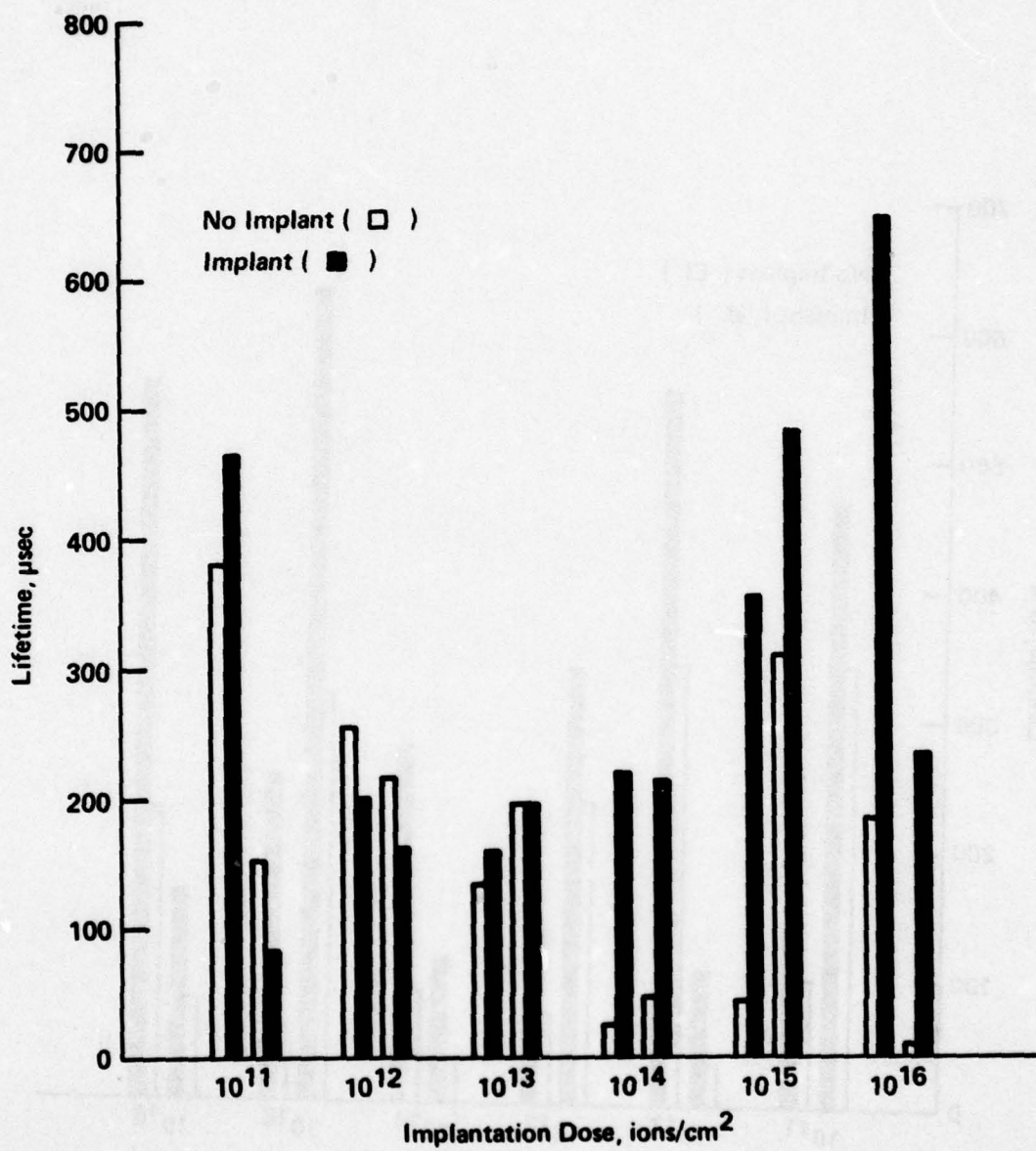


Fig. 1 Argon backside gettering. Minority carrier lifetime versus implantation dose. The lifetime values obtained inside and outside the implanted area are shown side by side for comparison.

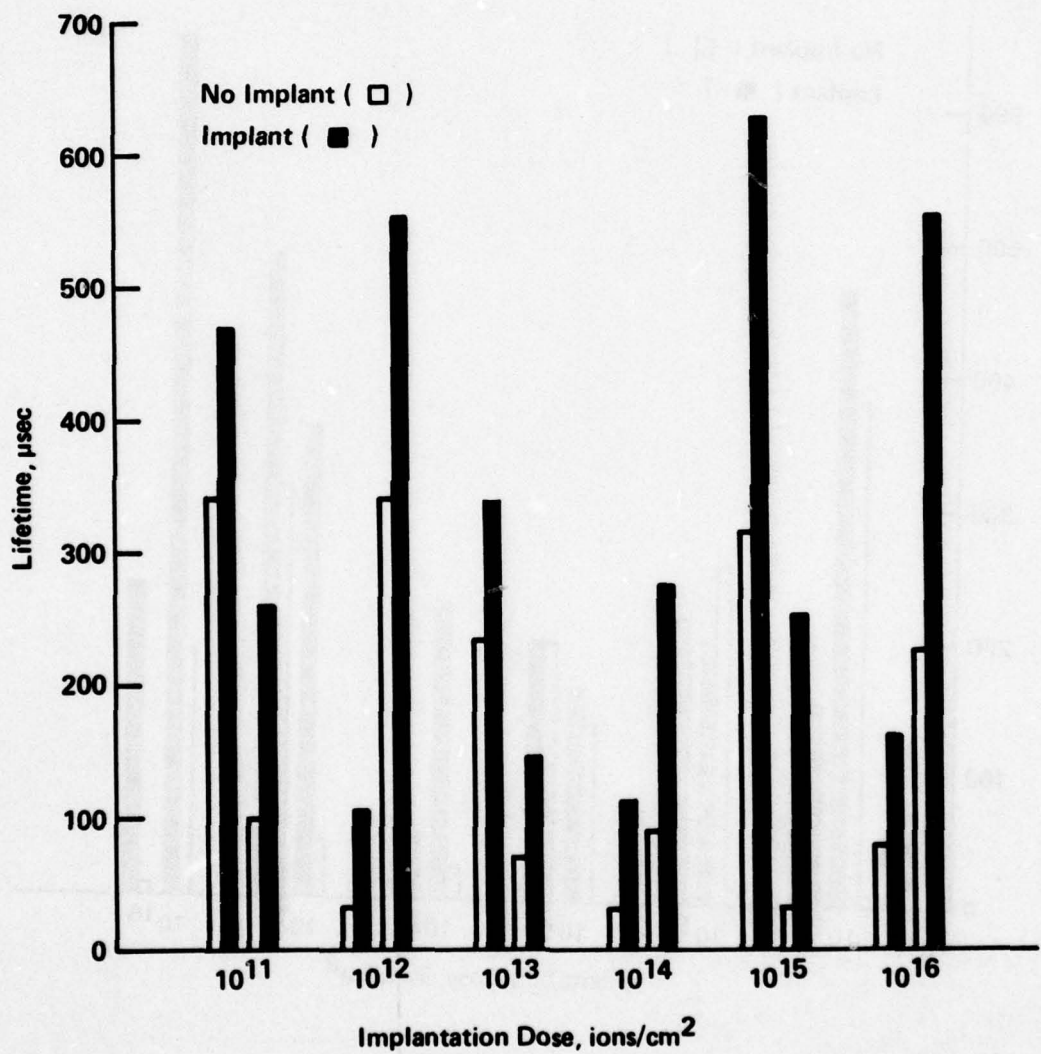


Fig. 2 Oxygen backside gettering. Minority carrier lifetime versus implantation dose. The lifetime values obtained inside and outside the implanted area are shown side by side for comparison.

For argon implantation, Figure 1 shows that a dose of 10^{13} ions/cm² or larger results in a substantial lifetime improvement.

For 2Mev oxygen gettering, a similar lifetime improvement can be seen (Fig. 2). However, lifetime improvement due to O⁺ implantation starts in this experiment at a dose as low as 10^{11} ions/cm². This effect is very surprising. Furthermore, the lifetime improvement does not show any clear dependency on implantation dose in contrast to the argon implantation.

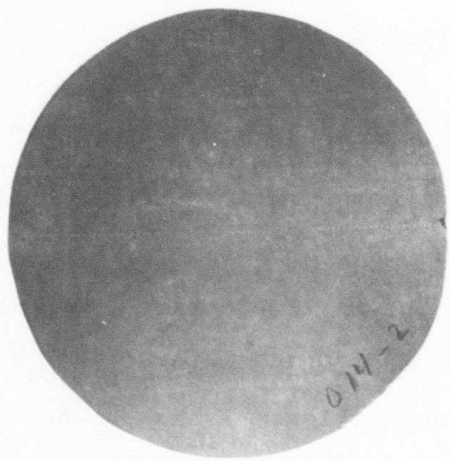
Damage Characterization

(a) X-ray Topographic Investigation

Transmission x-ray topography of O⁺ and Ar⁺ implanted wafers was used to investigate wafer perfection after implantation and again after MOS processing. For O⁺ implantation no damage contrast due to implantation can be resolved at a dose of 10^{13} ions/cm² and below. At 10^{14} ions/cm² and above, two contrast regions, 1 and 2, are observed as shown in Fig. 3(a). Region 1 corresponds to the non-implanted substrate, which is shielded against the ion beam. The contrast in Region 2 arises from the formation of a damaged layer below the surface. After MOS processing, the subsurface damage layer in the wafers implanted with 10^{14} ions/cm² recrystallizes and leaves no resolvable x-ray



(a)

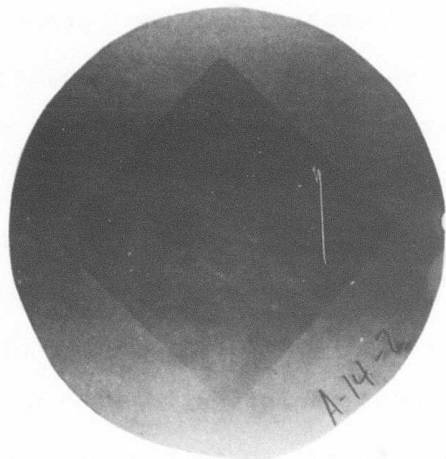


(b)

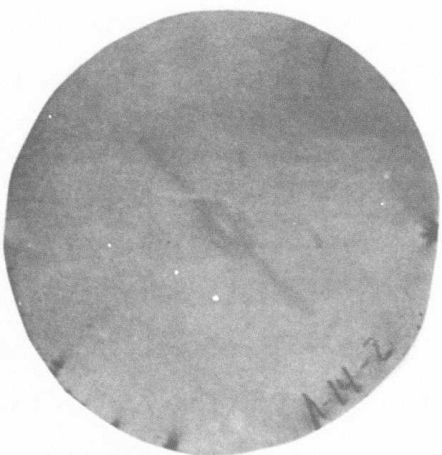
Fig. 3 X-ray topographs of a wafer implanted with
 $0^+ 10^{14}$ ions/cm². (a) as-implanted, and
(b) after MOS processing.

contrast, as shown in Fig. 3(b). However, the wafers implanted with 10^{15} and 10^{16} ions/cm² show no significant change in damage contrast after the processing, indicating that the damage has not yet been annealed out after the first oxidation treatment.

For Ar⁺ implantation, no damage x-ray contrast can be resolved at 10^{12} ions/cm² and below. At 10^{13} ions/cm², a weak damage contrasts similar to that of Fig. 3(a), is observed. As the dose increases to 10^{14} ions/cm² and above, the implanted wafers have three distinct contrast regions, 1, 2, and 3, as shown in Fig. 4(a). Region 1 corresponds to the non-implanted substrate. The contrast in Region 2 arises from formation of a continuous damaged layer. The fringe contrast in Region 3 is due to the maximum intensity of the non-uniform beam (6-8). Similar to O⁺ implantation, the damaged layer generated by Ar⁺ implantation recrystallizes during MOS processing. The degree of crystal perfection in the recrystallized layer depends upon implantation dose, or more precisely, on the extent of the implantation damage. At 10^{14} ions/cm², the recrystallized layer in Region 2 gives no residual damage contrast, while the layer in Region 3 shows residual damage contrast, Fig. 4(b). The residual contrast indicates the existence of crystal imperfections in Region 3. At 10^{15} and 10^{16} ions/cm², no significant contrast change is observed in these three regions after annealing through oxidation.



(a)



(b)

Fig. 4 X-ray topographs of a wafer implanted with Ar^+ 10^{14} ions/cm². (a) as-implanted, and (b) after MOS processing.

The three different contrast regions are characteristic of non-uniform Mev implantation damage. This damage has previously been studied in detail (6 - 8). It was shown that high energy implantation produces a sub-surface layer of heavily damaged silicon, which can be amorphous. This layer is buried into a silicon matrix of good crystalline perfection. Such a heavily damaged crystal can be compared to a bi-crystal, consisting of a perfect bulk and a perfect thin layer crystal, separated by a heavily damaged (amorphous) layer. A simple picture describing this damage model is shown in Fig. 5. The fringe contrast observed in the topographs in Region 3 arises from simultaneous diffraction of x-rays produced by such bi-crystals and can be used to study the annealing of the ion implantation damage in the crystal. (6-8)

(b) Transmission Electron Microscopy Investigation

The crystal defects in the damaged layer were also investigated through transmission electron microscopy (TEM). TEM specimen preparation requires first controlled removal of a surface layer on the implanted wafer side. The thickness of the surface layer to be removed is about $0.8\mu\text{m}$ for Ar^+ implanted samples and about $1.5\mu\text{m}$ for O^+ implanted samples. Subsequently, the specimens are jet etched from the non-implanted side until they are thin enough ($1\mu\text{m}$) for electron transmission.

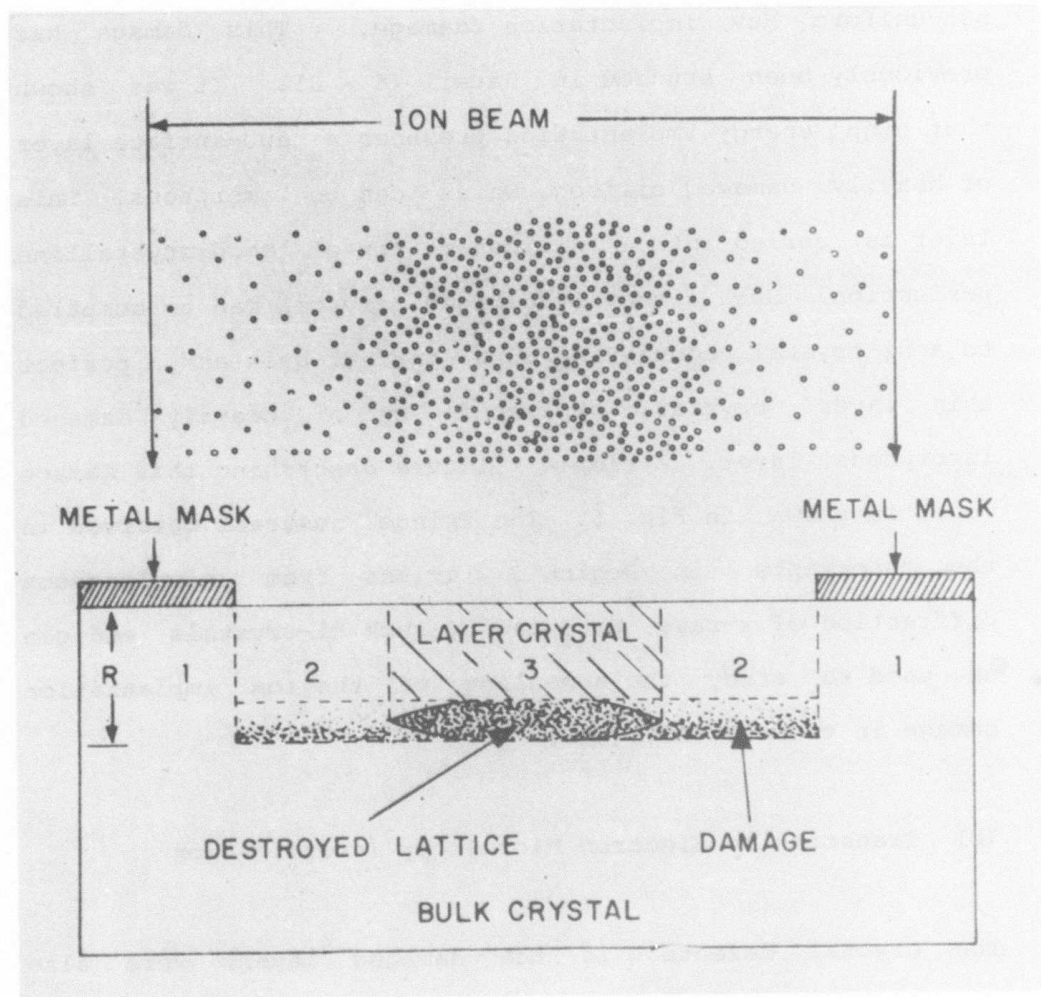


Fig. 5 Model of implantation damage in silicon after high energy bombardment.

TEM investigation show that the crystal defects that form during the annealing of the damaged layer as a result of MOS processing depend on the implantation dose and on the ion species. For Ar^+ implantation at and below 10^{13} ions/cm², no resolvable crystal defect can be detected. This is in good agreement with the results obtained by x-ray topography which show no residual damage contrast after MOS processing. At 10^{14} ions/cm², the implantation damage causes formation of stacking faults and dislocation loops during MOS processing, Fig. 6(a). The density of the faults and loops is about 1×10^6 per cm². With a dose of 10^{15} ions/cm², stacking faults, dislocation loops and networks are dominant defects, Fig. 6(b). The density of the faults and loops increases to about 4×10^8 per cm². In addition, argon bubbles of approximately $70\text{--}80\text{\AA}$ in size and of a density of 10^{10} per cm² are also observed. For an implantation dose of 1×10^{16} ions/cm², the dominant defects are dislocation networks and argon bubbles, Fig. 6(c). The size of the bubbles increases to $100\text{--}120\text{\AA}$.

For O^+ implantation at and below 10^{14} ions/cm² the damage anneals out during MOS processing. At 10^{15} ions/cm², dislocation loops and stacking faults are the dominant defects, Fig. 7(a). The loops are of two different sizes. One group is about 500\AA in size, and the other approximately

(c)



(b)



(a)



Fig. 6 TEM micrographs showing crystal defects in 1 MeV Ar^+ implanted silicon after MOS processing (a) 10^{14} ions/cm 2 , (b) 10^{15} ions/cm 2 , and (c) 10^{16} ions/cm 2 .

1000 ~ 2000 \AA large. At 10^{16} ions/cm 2 , stacking faults and damage clusters are predominant, Fig. 7(b). The size of these clusters is about 150 \AA .

For both Ar $^+$ and O $^+$ implantation, the formation of these crystal defects starts from the implanted damaged layer. The crystal defects formed are confined to a well defined layer located between the bulk crystal and a thin surface layer which is also of good crystal perfection. The bulk crystal perfection is recognized from the observation that no defects are detected at a depth beyond 2 μm for Ar $^+$ implanted samples, and beyond 3 μm for O $^+$ implanted samples. The thin layer crystal of the surface is also found to be defect-free. This result is shown in Fig. 7(c) for a sample implanted with 2Mev O $^+$ at 10^{16} ions/cm 2 . Fig. 7(c) shows that the defect density decreases as the sample thickness decreases, or as the sample approaches the surface layer. The damage profile, as found by TEM investigation, is consistent with the model shown in Fig. 5.

(c) Preferential Etching

The front surface of the wafers, after MOS lifetime measurements, was also investigated by preferential etching. Etching reveals only a relatively low density of stacking faults, typically 10^2 to 10^3 per cm 2 , in the non-gettered area. In the gettered area, above the backside implantation, such faults are practically absent.

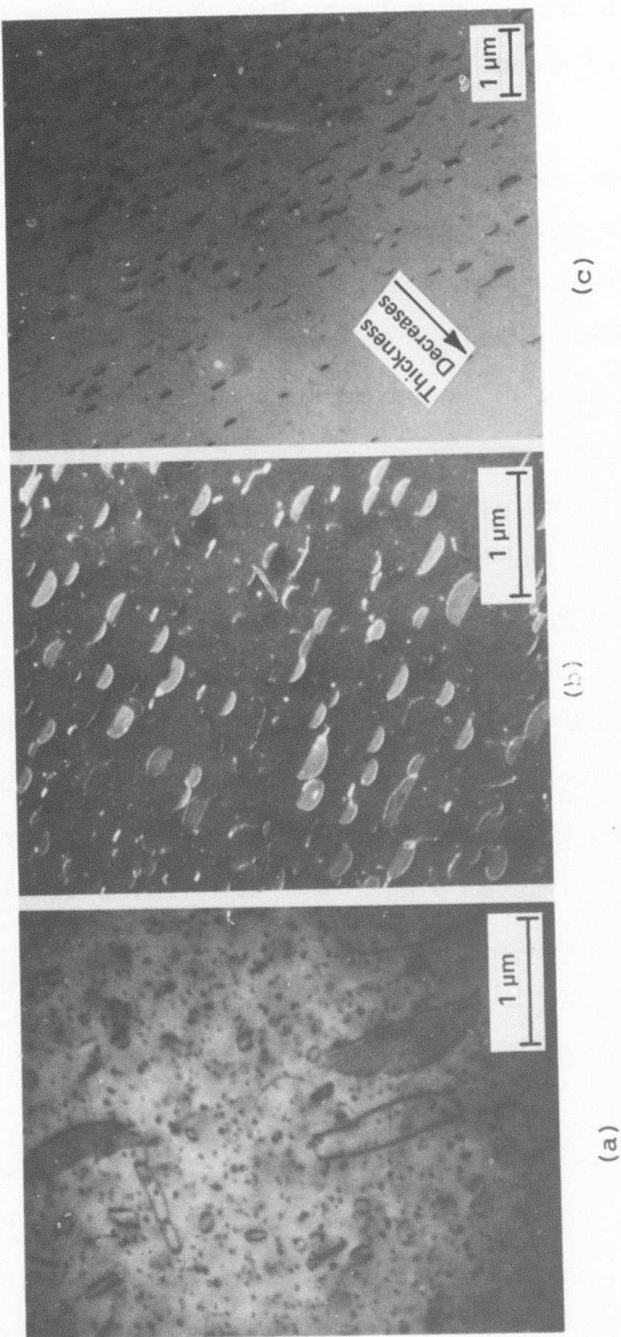


Fig. 7 TEM micrographs showing crystal defects in 2 Mev 0^+ implanted silicon after MOS processing.
 (a) 10^{15} ions/cm², (b) and (c) 10^{16} ions/cm².
 Fig. (c) shows the defect density decreases as the sample thickness decreases.

DISCUSSION

The measurements indicate that substantial improvement in minority carrier lifetime in silicon can be achieved through high energy Ar^+ and O^+ implantation gettering. The dependence of lifetime improvement on implantation dose is different for Ar^+ and O^+ implantation. For Ar^+ gettering, lifetime improvement is observed to start at a dose of 10^{14} ions/cm² and above. For O^+ gettering the lifetime improvement occurs at a dose as low as 10^{11} ions/cm². Based on such findings, we assume that the dominant gettering mechanisms for Ar^+ and O^+ gettering are different.

As shown in the literature gettering can arise from strain and/or ion pairing (3,5). The use of strain fields as gettering sites has found application in mechanical damage gettering (11,12), implantation damage gettering (1-5) and surface layer deposition gettering (13). Ion pairing is found to be responsible for phosphorous diffusion gettering (3,5).

For Ar^+ implantation, the improvement in lifetime obtained can be explained as a result of strain gettering. As shown in the x-ray topographs of Fig. 4, significant implantation damage is observed for a dose of 10^{14} ions/cm² and above.

TEM investigation, Fig. 6, shows that as a result of such damage, extended crystal defects are induced in the damaged layer during MOS processing.

These results indicate that only those wafers, which have either sufficient implantation damage or residual crystal defects, improve lifetime as shown in Fig. 1. The minimum dose for such gettering to occur is about 10^{14} ions/cm². This dose corresponds to the amorphization dose of Ar⁺ implantation. This suggests that for Ar⁺ gettering to be effective, damage in the silicon lattice has to reach the amorphous state.

Gettering efficiency of argon, as determined from the ratio of lifetime between the implanted and the non-implanted parts, seems to increase with both implantation dose and damage. This can be seen in Fig. 1 for low lifetime wafers (<50 μ sec) implanted at a dose of 10^{14} ions/cm² and above. The increase of implantation damage with ion dose is evident from the TEM micrographs of Fig. 6 and the x-ray topographs of Fig. 4. The results of lifetime measurements and damage characterization indicate again that the annealing of the implantation damage is the driving mechanism during argon gettering.

Contrary to the results obtained for argon gettering, where the gettering efficiency is found to be dose dependent,

oxygen gettering does not show such a dependency on implantation dose. Surprising is that an implantation dose of 10^{11} O^+/cm^2 already gives a strong improvement in lifetime. Damage characterization of oxygen implanted samples detects no defects due to implantation a) in the as-implanted state up to 10^{13} O^+/cm^2 and b) after MOS processing up to 10^{14} O^+/cm^2 . These results indicate that oxygen is capable of a gettering action independent of lattice damage which seems to be necessary if argon is used. These results are interesting if viewed in the context of the results reported in Chapter I of this report. In this work we found that degradation of lifetime due to ion implantation is always less if the implantation is done through an oxide layer. We speculated that oxygen ions, which are transferred by "knock-on" from the oxide layer into the silicon substrate are thus instrumental in retarding lifetime degradation due to the argon or silicon implantation.

To substantiate and verify the oxygen results we stripped the MOS metallurgy and the oxide from all oxygen implanted wafers and MOS processed the same wafers including the control wafers for a second time. Again we find that oxygen implanted wafer areas give better lifetime as found after the first MOS processing. This experiment does not only verify the first results but indicates also that high energy implantations are active during a second heat-treatment.

The results of the second MOS processing are summarized in Fig. 8(a) and 8(b).

SUMMARY

High energy argon and oxygen implantations on wafer backsides improve minority carrier lifetimes measured by the MOS C-t technique on wafer front sides.

High energy implantations produce buried damage layers under the silicon surface. Such buried damage layers are resistant to annealing cycles as encountered during standard semiconductor processing. Consequently, they provide more efficient gettering action as compared to damage layers produced by low energy implantations.

High energy argon gettering is found to be dependent on the implantation dose. Maximum gettering efficiency is obtained for high dose implantation ($>10^{14} \text{ Ar}^+/\text{cm}^2$) which leads to the formation of sub-surface amorphous layers.

Contrary oxygen gettering shows no clear dose dependency. A remarkable gettering efficiency is already obtained for an implantation dose of $10^{11} \text{ O}^+/\text{cm}^2$.

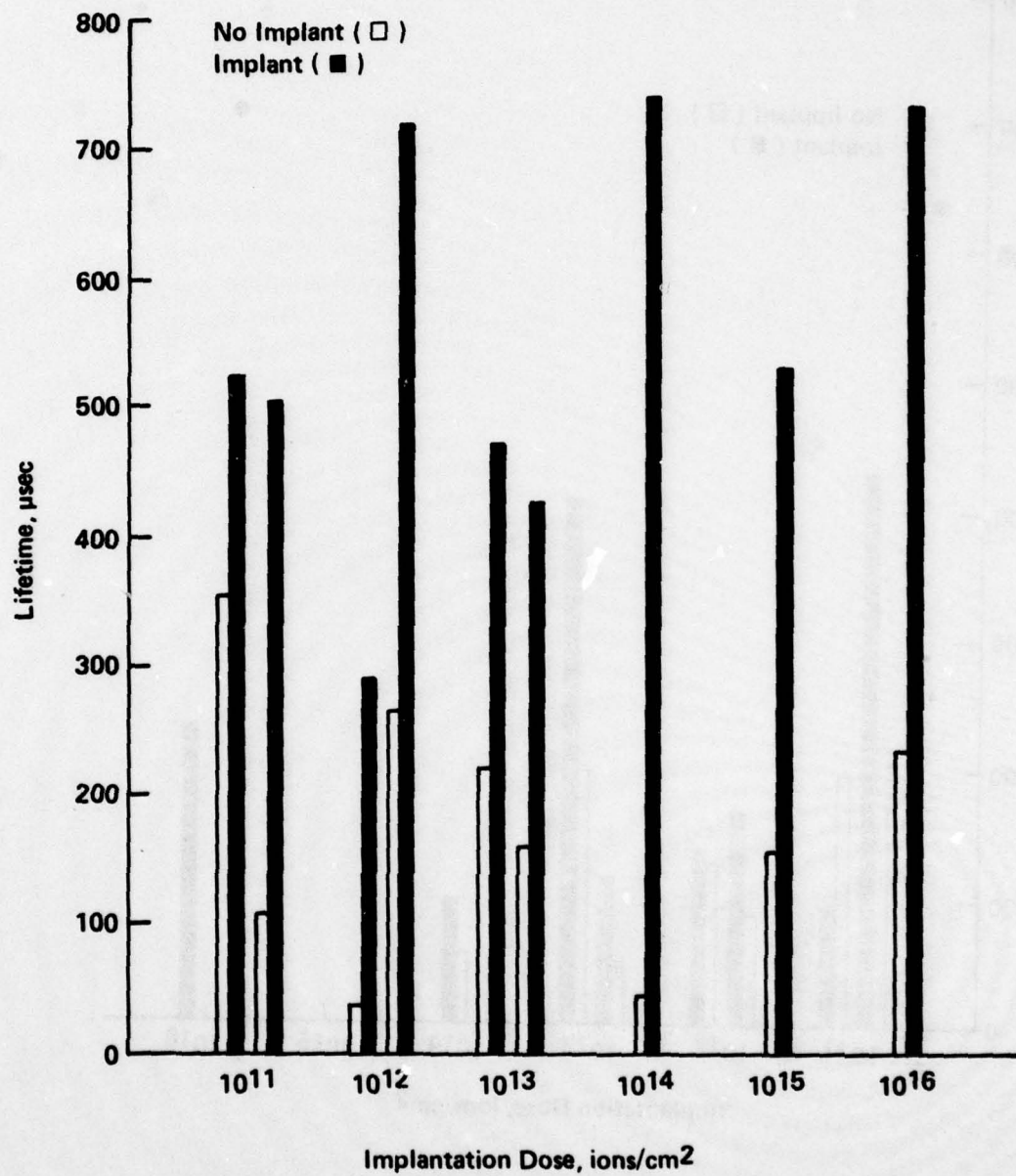


Fig. 8(a) Lifetime of O^+ gettered silicon after the second oxidation.

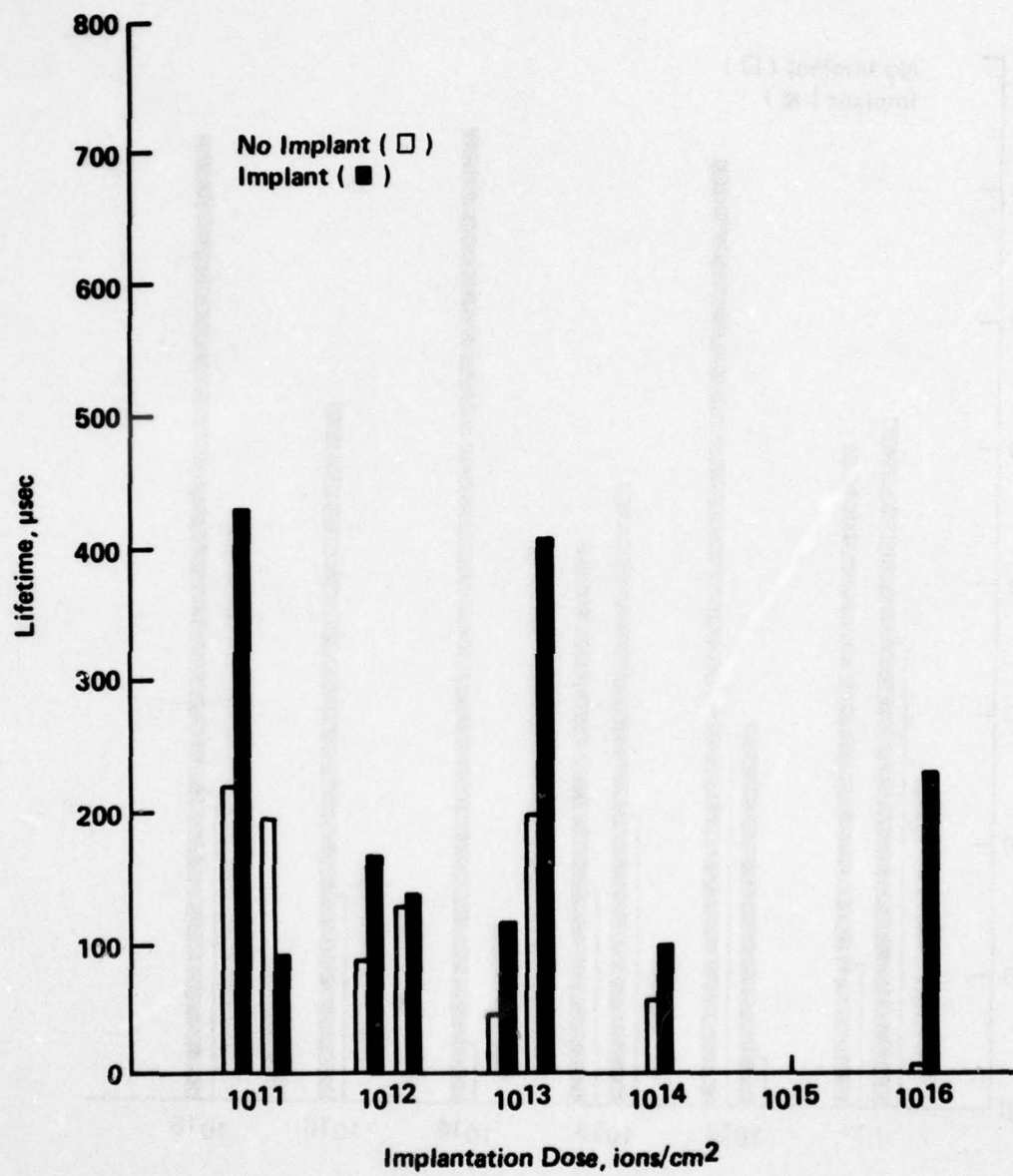


Fig. 8(b) Lifetime of Ar^+ gettered silicon after the second oxidation.

REFERENCES

1. B. Masters and J. Fairfield, *Radiation Effects*, 6, 57 (1970).
2. C. M. Hsieh, J. R. Mathews, H. D. Seidel, K. A. Picker and C. M. Drum, *Appl. Phys. Lett.*, 22, 238 (1973).
3. T. E. Seidel, R. L. Meek and A. G. Cullis, *J. Appl. Phys.*, 46, 600 (1975).
4. M. R. Poponiak, T. Nagasaki, and T. H. Yeh, *J. Electrochem. Soc.*, 124, 1802 (1977).
5. W. F. Tseng, T. Koji, J. W. Mayer and T. E. Seidel, *Appl. Phys. Lett.*, 33, 442 (1978).
6. U. Bonse, M. Hart, and G. H. Schwuttke, *Phys. Stat. Sol.*, 33, 361 (1969).
7. G. H. Schwuttke and K. Brack, *Trans. of the Met. Soc. AIME*, 245, 475 (1969).

8. E. H. te Kaat and G. H. Schwuttke, in "Advances in X-ray Analysis," Ed. K.F.J. Heinrich, Vol. 15, p.504, Plenum Press, N.Y. (1972).
9. W. S. Johnson and J. F. Gibbons, "Projected Range Statistics in Semiconductors," Stanford University (1969).
10. H. F. Kappert, K. F. Heidemann, B. Grabe, and E. te Kaat, Phys. Stat. Sol. (a) 47, 451 (1978).
11. J. E. Lawrence, Trans. of the Met. Soc. AIME, 484, 242 (1968).
12. G. H. Schwuttke, K. Yang, and H. Kappert, Phys. Stat. Sol. (a) 42, 553 (1977).
13. P. M. Petroff, G. A. Rozgonyi, and T. T. Shang, J. Electrochem. Soc., 123, 565 (1976).
14. T. Y. Tan, E. E. Gardner, and W. K. Tice, Appl. Phys. Lett., 30, 175 (1977).

15. W. Fahrner and C. P. Schneider, Electro. Chem. Soc. J. 123, 100, (1976).
16. K. Graff and H. Pieper, J. Electronic Mat'l, 4, 2, 281 (1975).
17. K. H. Yang, G. H. Schwuttke, and H. Kappert, Phys. Stat. Sol. (a) 50, 221, 1978.